

LOCAL SIMULATIONS OF SPIRAL GALAXIES WITH THE TIGRESS FRAMEWORK: I. STAR FORMATION AND ARM SPURS/FEATHERS

WOONG-TAE KIM

Department of Physics & Astronomy, Seoul National University, Seoul 08826, Republic of Korea and
Department of Astrophysical Sciences, Princeton University, Princeton, NJ 08544, USA

CHANG-GOO KIM

Department of Astrophysical Sciences, Princeton University, Princeton, NJ 08544, USA

EVE C. OSTRIKER

Department of Astrophysical Sciences, Princeton University, Princeton, NJ 08544, USA

Accepted for publication in the ApJ

ABSTRACT

Spiral arms greatly affect gas flows and star formation in disk galaxies. We use local three-dimensional simulations of the vertically-stratified, self-gravitating, differentially-rotating, interstellar medium (ISM) subject to a stellar spiral potential to study the effects of spiral arms on star formation and formation of arm spurs/feathers. We adopt the TIGRESS framework of Kim & Ostriker (2017) to handle radiative heating and cooling, star formation, and ensuing supernova (SN) feedback. We find that more than 90% of star formation takes place in spiral arms, but the global star formation rate (SFR) in models with spiral arms is enhanced by less than a factor of 2 compared to the no-arm counterpart. This results from a quasi-linear relationship between the SFR surface density Σ_{SFR} and the gas surface density Σ , and supports the picture that spiral arms do not trigger star formation but rather concentrate star-forming regions. Correlated SN feedback produces gaseous spurs/feathers downstream from arms in both magnetized and unmagnetized models. These spurs/feathers are short-lived and have magnetic fields parallel to their length, in contrast to the longer-lived features with perpendicular magnetic fields induced by gravitational instability. SN feedback drives the turbulent component of magnetic fields, with the total magnetic field strength sublinearly proportional to Σ . The total midplane pressure varies by a factor of ~ 10 between arm and interarm regions but agrees locally with the total vertical ISM weight, while Σ_{SFR} is locally consistent with the prediction of pressure-regulated, feedback-modulated theory.

Keywords: galaxies: ISM — galaxies: star formation — galaxies: spiral — galaxies: structure — ISM: kinematics and dynamics — ISM: magnetic fields — magnetohydrodynamic (MHD) — stars: formation

1. INTRODUCTION

Spiral arms are of paramount importance in dynamical and chemical evolution of disk galaxies (e.g., Buta & Combes 1996; Kormendy & Kennicutt 2004; Sellwood 2014). They not only exert non-axisymmetric torques to drive secular migration of stars and gas clouds (e.g., Roškar et al. 2008; Bovy et al. 2012; Daniel & Wyse 2015, 2018), but also compress gas to aid the formation of giant molecular clouds (GMCs) in them (e.g., Elmegreen & Elmegreen 1983; Rand 1993; Elmegreen 1993; see also Dobbs & Baba 2014). They are also sites of active star formation (e.g., Elmegreen & Elmegreen 1986; Foyle et al. 2010; Elmegreen 2011; Schinnerer et al. 2017; Leroy et al. 2017) and are associated with spurs or feathers that extend nearly perpendicularly from arm to interarm regions¹ (e.g., Sandage 1961; Lynds 1970; Elmegreen 1980;

Scoville et al. 2001; La Vigne et al. 2006; Muraoka et al. 2009; Schinnerer et al. 2013, 2017; Puerari et al. 2014; Koo et al. 2017; Elmegreen et al. 2018; Elmegreen & Elmegreen 2019).

Massive stars formed inside spiral arms – and in arm spurs/feathers – profoundly affect the physical properties of the surrounding interstellar medium (ISM) by supplying feedback in the form of stellar winds and radiation during their lifetime and via supernova (SN) explosions at their death (e.g., McKee & Ostriker 2007; Krumholz et al. 2014). SN feedback appears strongest among various mechanisms that contribute to driving turbulence in the ISM (e.g., Mac Low & Klessen 2004), and is a major agent for regulating galactic star formation rates (SFRs) (e.g., Ostriker et al. 2010; Ostriker & Shetty 2011; Kim et al. 2011).

One of the long-standing issues with disk galaxies is whether spiral arms trigger star formation or just organize star-forming regions into an arm shape. The conventional wisdom was that spiral arms enhance SFRs

wkim@astro.snu.ac.kr,
eco@astro.princeton.edu

cgkim@astro.princeton.edu,

¹ More precisely, in the observational literature the term *feathers* has been used to refer to dust features seen as dark against a bright background, while *spurs* indicates luminous stellar features in optical light (see, e.g., La Vigne et al. 2006; Schinnerer et al. 2017). Spurs most likely correspond to dense feathers with recent

star formation. In this paper, we use the two terms interchangeably.

by compressing gas clouds above the threshold density for gravitational collapse (e.g., Roberts 1969; Shu et al. 1973; Roberts et al. 1975). Cepa & Beckman (1990) argued in favor of this notion based on arm *vs.* interarm star formation efficiency (SFE) in atomic gas in M74 and M109 and typical arm/interarm molecular density contrasts (see also Lord & Young 1990; Knapen et al. 1996; Seigar & James 2002). However, there does not in fact seem to be a threshold for star formation in molecular gas (Schruba et al. 2011), and Elmegreen & Elmegreen (1986) found no obvious correlation between the mean SFRs and the arm strength, indicating that spiral arms are not needed to trigger star formation. A more recent study of Foyle et al. (2010) for galaxies M51 and M74 showed that the SFE within molecular gas is almost similar (within $\sim 10\%$) in the arm and interarm regions. Given that the SFR is not correlated with the atomic gas but with the molecular gas (Bigiel et al. 2008; Leroy et al. 2008, 2013), the existing observational results favor the idea of star-formation organization (rather than triggering) by spiral arms.

Another interesting issue regarding spiral arms is what mechanism accounts for the formation of gaseous spurs/feathers. A number of processes have been put forward to explain spur/feather formation (see, e.g., Shu 2016 and references therein). For example, Balbus (1988) argued that swing amplification of hydrodynamic perturbations inside spiral arms is responsible for spurs/feathers, while the presence of magnetic fields appears essential to promote the fast growth of self-gravitating perturbations in spiral arms (e.g., Elmegreen 1993; Kim & Ostriker 2002, 2006; Shetty & Ostriker 2006, 2008; Lee & Shu 2012; Lee 2014). In particular, Kim & Ostriker (2002, 2006) ran magnetohydrodynamic (MHD) simulations of local shearing-box models under an isothermal approximation and showed that elongated spur structures grow via magneto-Jeans instability (MJ), in which magnetic fields remove angular momentum from self-gravitationally contracting regions. In these simulations, gaseous spurs undergo gravitational fragmentation into bound clumps within one or two orbits. When driven by MJ, the mean spacing between spurs along the arm is determined by the Jeans length at the density peak of spiral arms.

There have also been mechanisms proposed for spur/feather formation that do not rely on gaseous self-gravity and magnetic fields. Wada & Koda (2004) ran non-self-gravitating simulations and showed that hydrodynamic spiral shocks are unstable to clump-forming, wiggle instability (WI; see also Renaud et al. 2013), which later turns out to arise due to generation of potential vorticity (PV) at perturbed shock fronts that gas passes through periodically (Kim et al. 2014, 2015; Sormani et al. 2017). Using smoothed particle hydrodynamics (SPH) simulations, Dobbs & Bonnell (2006) found that changes of angular momenta at shock fronts make the orbits of cold particles crowded, resulting in clumps and feathers behind the shocks.

Although the numerical studies mentioned above were useful to understand physical processes involved in spiral shocks and structure formation inside spiral arms, almost all of them were limited to isothermal models without considering star formation and SN feedback. Realistically, the dominant pressure in the ISM is not

thermal pressure but turbulent pressure. Since SN feedback drives turbulence and also creates larger-scale structures including superbubbles (e.g., McCray, & Snow 1979; Tomisaka et al. 1981), it may also control spur/feather formation at least partially. Indeed, Schinnerer et al. (2017) found that feathers in M51 are deeply associated with massive star clusters and suggested that their shape and evolution should be influenced by stellar feedback. Therefore, it is necessary to explore how spiral arm substructures form and evolve in a medium continually stirred by SN feedback.

Several recent works have incorporated stellar feedback in global numerical simulations of spiral galaxies and observed spur formation (e.g., Renaud et al. 2013; Baba et al. 2017; Pettitt et al. 2017). From a hydrodynamic simulation of a Milky Way-like galaxy, Renaud et al. (2013) suggested that spurs/feathers originate from velocity shear near spiral arms. Using N -body/SPH simulations for galaxies with steady or dynamic spirals, Baba et al. (2017) found that GMCs formed by cloud-cloud collisions inside arms are sheared into feathers in interarm regions (see also Dobbs et al. 2017). Pettitt et al. (2017) ran models in which spiral arms are driven by a tidal encounter with a companion galaxy (see also Tress et al. 2020). They found that spurs/feathers are much larger and stronger in outer arms (bridges to the companion) that have higher SFRs than inner arms. They also found that feathers are located in between young star clusters in the interarm regions, suggesting that stellar feedback somehow affects the formation and evolution of interarm feathers. These diverse results on spur/feather formation in numerical simulations indicate that there is no consensus as to how star formation and feedback influence these features.

In this paper, we run local three-dimensional simulations of vertically-stratified, self-gravitating, differentially-rotating, magnetized, galactic gaseous disks under the influence of a stellar spiral potential. To handle star formation and SN feedback, we adopt the TIGRESS (Three-phase Interstellar medium in Galaxies Resolving Evolution with Star formation and Supernova feedback) algorithms developed by Kim & Ostriker (2017). The TIGRESS framework features multi-physics modules including gas accretion to sink/stellar particles and delayed SN feedback in the form of thermal energy and/or momentum, and allows self-consistent simulations of the three-phase star-forming ISM. The present study extends the model setup of Kim & Ostriker (2017) by including a local stellar spiral-arm potential. Our work also extends the isothermal models of Kim & Ostriker (2002, 2006) by considering radiative cooling and heating, star formation, and stellar feedback (supernovae and FUV heating).

This work has several objectives. First, we want to understand the role of spiral arms on galactic star formation, addressing the issue of star-formation triggering or organization by spiral arms. Second, we wish to investigate the effects of SN feedback on gaseous spur formation and evolution, for which it is essential to utilize the TIGRESS algorithms. In addition, spiral structure imposes spatial variations in mean properties that reflect a temporal sequence as gas flows from arm to interarm conditions and back. Once the simulation reaches a quasi-steady state, it is interesting to calculate profiles

of various physical quantities such as the mean gas surface density, SFR, magnetic field strength, and midplane stresses as functions of the distance downstream from the spiral arm peak, and to explore correlations among these physical variables.

The remainder of the paper is organized as follows. In Section 2, we describe our numerical methods and the models we consider, including briefly summarizing the TIGRESS framework for treating star formation and SN feedback. In Section 3, we present the temporal and morphological evolution of our models, with a focus on spur formation. In Section 4, we present the spatial profiles and correlations of various physical quantities as well as the temporal variations of volume-integrated quantities including SFR and mass fractions. In Section 5, we summarize our results and discuss their astronomical implications.

2. METHODS

In this paper we study evolution of the ISM in a vertically-stratified disk under the influence of a stellar spiral potential as well as star formation and SN feedback. Similar work without a spiral potential was reported by Kim & Ostriker (2017), while an isothermal version without star formation and feedback was studied by Kim & Ostriker (2002, 2006). In this section, we present the equations we solve, the numerical methods, and the model parameters we adopt.

2.1. Basic Equations

We consider a Cartesian box that is corotating with a local segment of a stellar spiral potential. The spiral potential is assumed to be tightly wound with a pitch angle $\sin i \ll 1$ and rigidly rotating at a constant pattern speed Ω_p about the center of a galaxy. The local Cartesian frame is centered at a position $(R_0, \phi_0 = \Omega_p t, z_0 = 0)$ in the galactic plane and inclined such that $\hat{\mathbf{x}}$ and $\hat{\mathbf{y}}$ point toward the directions perpendicular and parallel to the arm, respectively, while $\hat{\mathbf{z}}$ corresponds to the direction perpendicular to the galactic plane (e.g., Roberts 1969; Balbus 1988). This local spiral-arm frame is advantageous for capturing essential physics associated with rotational shear and the spiral potential while affording much higher resolution than global models of spiral galaxies. Our simulation domain is a rectangular parallelepiped with size $L_x \times L_y \times L_z$, where $L_x = 2\pi R_0(\sin i)/m$ is equal to the arm-to-arm distance for an m -armed spiral. In this local frame, the background velocity arising from galactic differential rotation is given by

$$\mathbf{v}_0 = R_0(\Omega_0 - \Omega_p) \sin i \hat{\mathbf{x}} + [R_0(\Omega_0 - \Omega_p) - q\Omega_0 x] \hat{\mathbf{y}}, \quad (1)$$

where $\Omega_0 = \Omega(R_0)$ is the angular velocity at R_0 in the inertial frame and $q \equiv -(d \ln \Omega / d \ln R)|_{R_0} = 1$ is the shear parameter for a flat rotation curve (e.g., Kim & Ostriker 2002).

The ideal MHD equations expanded in the local frame

read

$$\frac{\partial \rho}{\partial t} + \nabla \cdot (\rho \mathbf{v}) = 0, \quad (2)$$

$$\frac{\partial(\rho \mathbf{v})}{\partial t} + \nabla \cdot \left[\rho \mathbf{v} \mathbf{v} + \left(P + \frac{B^2}{8\pi} \right) \mathbf{I} - \frac{\mathbf{B} \mathbf{B}}{4\pi} \right] = -2\rho \Omega_0 \times (\mathbf{v} - \mathbf{v}_0) - \rho \nabla(\Phi_{\text{self}} + \Phi_{\text{ext}}), \quad (3)$$

$$\frac{\partial E}{\partial t} + \nabla \cdot \left[\left(E + P + \frac{B^2}{8\pi} \right) \mathbf{v} - \frac{\mathbf{B}(\mathbf{B} \cdot \mathbf{v})}{4\pi} \right] = -\rho \mathbf{v} \cdot \nabla(\Phi_{\text{self}} + \Phi_{\text{ext}}) - \rho \mathcal{L}, \quad (4)$$

$$\frac{\partial \mathbf{B}}{\partial t} = \nabla \times (\mathbf{v} \times \mathbf{B}), \quad (5)$$

$$\nabla^2 \Phi_{\text{self}} = 4\pi G(\rho + \rho_{\text{sp}}). \quad (6)$$

Here, \mathbf{I} is the identity matrix, $E = \rho v^2/2 + P/(\gamma - 1) + B^2/8\pi$ is the total energy density, $\rho \mathcal{L}$ is the net cooling rate per unit volume per unit time, Φ_{ext} is the external gravitational potential, and Φ_{self} is the self-gravitational potential of gas with density ρ and star particles with density ρ_{sp} . The other symbols have their usual meaning. The first two terms in the right-hand side of Equation (3) denote, respectively, the Coriolis force and the term counterbalancing the advection of the y -velocity along the x -direction in the background flow.

The external gravitational potential Φ_{ext} in Equation (3) consists of three parts as $\Phi_{\text{ext}} = \Phi_* + \Phi_{\text{dm}} + \Phi_{\text{arm}}$, where

$$\Phi_*(z) = 2\pi G \Sigma_* z_* \left[\left(1 + \frac{z^2}{z_*^2} \right)^{1/2} - 1 \right], \quad (7)$$

$$\Phi_{\text{dm}}(z) = 2\pi G \rho_{\text{dm}} R_0^2 \ln \left(1 + \frac{z^2}{R_0^2} \right), \quad (8)$$

$$\Phi_{\text{arm}}(x) = \Phi_{\text{arm}}(0) \cos \left(\frac{2\pi x}{L_x} \right), \quad (9)$$

respectively representing the fixed gravitational potentials from the stellar disk with surface density Σ_* and scale height z_* , dark matter halo with mass density ρ_{dm} , and the stellar spiral arm with amplitude $\Phi_{\text{arm}}(0)$.

For the net cooling function in Equation (4), we take

$$\rho \mathcal{L} = n_{\text{H}}^2 \Lambda(T) - n_{\text{H}} \Gamma, \quad (10)$$

where $n_{\text{H}} = \rho/(\mu m_{\text{H}})$ is the number density of hydrogen nuclei, with $\mu(T)$ being the mean molecular weight: we allow μ to vary with T from $\mu_{\text{ato}} = 1.295$ (for fully neutral gas) to $\mu_{\text{ion}} = 0.618$ (for fully ionized gas). For the cooling rate $\Lambda(T)$, we adopt the fitting formula of Koyama & Inutsuka (2002) for $T < 10^{4.2}$ K (see also Kim et al. 2008), and for $T > 10^{4.2}$ K we adopt the collisional ionization equilibrium cooling function at solar metallicity from Sutherland & Dopita (1993).

The major heating source for warm and cold gas is the photoelectric effect of dust grains exposed to far ultraviolet (FUV) radiation. The FUV radiation includes the metagalactic radiation as well as the one emitted from young massive stars. To allow for the heating by young stars formed in our simulations, we calculate the mean FUV luminosity Σ_{FUV} from all star particles averaged over the simulation domain, and use it to evaluate the

time-varying heating rate Γ as

$$\frac{\Gamma}{\Gamma_0} = \frac{\mu(T) - \mu_{\text{ion}}}{\mu_{\text{ato}} - \mu_{\text{ion}}} \left[0.0024 + \frac{\Sigma_{\text{FUV}}}{\Sigma_{\text{FUV},0}} \frac{1 - E_2(\tau_{\perp}/2)}{\tau_{\perp}} \right]. \quad (11)$$

Here, $\tau_{\perp} = \kappa_{\text{FUV}} \Sigma$ with $\kappa_{\text{FUV}} = 10^3 \text{ cm}^3 \text{ g}^{-1}$ is the UV optical depth in the global plane-parallel approximation, and E_2 is the exponential integral function of order 2; this form represents global attenuation in the plane-parallel approximation. For the normalization factors in Equation (11), we take the heating rate $\Gamma_0 = 2 \times 10^{-26} \text{ erg s}^{-1}$ in the solar neighborhood (Koyama & Inutsuka 2002), the interstellar radiation field $\Sigma_{\text{FUV},0} = 2.1 \times 10^{-4} \text{ erg s}^{-1} \text{ cm}^{-2}$ (Draine 1978), and the contribution of the metagalactic FUV amounting to 0.24% (Sternberg et al. 2002). The photoelectric heating is completely turned off at high temperature ($T \gtrsim 10^5 \text{ K}$) where $\mu = \mu_{\text{ion}}$. While we do not include heating by photoionization, it would not make a significant difference in T compared to that from the photoelectric heating.

2.2. Star Formation and Feedback

We adopt the TIGRESS framework of Kim & Ostriker (2017) to treat star formation and SN feedback. Here we briefly summarize the TIGRESS algorithms: the reader is referred to Kim & Ostriker (2017) for the complete description. We note from the outset that in the present work we consider SN feedback alone, while ignoring early feedback (e.g., stellar winds, ionizing radiation). This implicitly assumes that the dynamical time in the surrounding clouds is longer than $\sim 4 \text{ Myr}$, so that SN feedback dominates early feedback, which is valid for the moderate-density environment under consideration.

In TIGRESS, star formation is modelled by creating a sink/star particle when a cell meets three conditions simultaneously: (1) its density exceeds the Larson-Penston threshold density, (2) it lies at a local potential minimum, and (3) its velocity is converging in all three directions (Gong & Ostriker 2013). The initial mass of the sink particle is set equal to the difference between the gas mass in the surrounding 3^3 -cell control volume prior to sink formation, and the mass in this region based on the extrapolation of the surrounding density field. Each sink particle is allowed to accrete mass and momentum from the surrounding gas over time, at a rate based on the fluxes through the surfaces of the control volume centered at the sink particle. When star particles are actively accreting, physical quantities such as density and velocity (except magnetic fields) in the cells inside the control volume are set as ghost zones based on the surrounding active cells. Sink particles represent star clusters with stellar populations that average over the initial mass function (IMF), with an age that reflects the accretion history. The immediate formation of a sink particle implicitly assumes that the timescale for gravitational collapse and star formation is shorter than the dynamical time of the surrounding gas, and that the star formation efficiency is high. Particles are merged if their control volumes overlap with each other, with physical quantities set by mass-weighted averages.

Sink/star particles age with time, with the mass-weighted mean age t_m updated to account for accreted gas. Particles are categorized into three species depend-

ing on t_m relative to the mean SN onset time $t_{\text{SN}} \sim 4 \text{ Myr}$ (determined stochastically for each particle) and the feedback lifetime $t_{\text{life}} = 40 \text{ Myr}$: (1) “growing” particles if $0 < t_m < t_{\text{SN}}$, (2) “feedback” particles if $t_{\text{SN}} < t_m < t_{\text{life}}$, and (3) “passive” particles if $t_{\text{life}} < t_m$. Growing particles are treated as sinks that contribute to the overall FUV radiation field and exert gravity. Feedback particles do not accrete and merge, but exert gravity and supply FUV radiation and SN feedback. Passive particles neither accrete nor supply feedback, but merely exert gravity on the gas and other particles.

For feedback particles with mass m_{sp} , the number of SN events expected over the time step Δt is drawn from the population synthesis model STARBURST99 (Leitherer et al. 1999), which is roughly $\mathcal{N}_{\text{SN}} \sim m_{\text{sp}} \Delta t / (m_* t_{\text{life}})$, where $m_* = 95.5 M_{\odot}$ is the mass of a star cluster per SN for a fully sampled Kroupa (2001) IMF. In each time step, we generate a uniform random number $\mathcal{U}_{\text{SN}} \in (0, 1)$ and turn on SN feedback only if $\mathcal{N}_{\text{SN}} > \mathcal{U}_{\text{SN}}$. We also consider SN events from runaway OB stars, by taking a binary fraction $f_{\text{bin}} \equiv 2/3$. If the event is determined to occur in a binary, we spawn a massless particle with initial velocity distribution taken from Eldridge et al. (2011) and let it explode after a certain delay time (to ensure the entire SN rate the same).

The mode of SN feedback that is implemented for any given event depends on the local density in the region around the SN. We start by adopting an initial radius $R_{\text{snr}} = 3\Delta x$ (for grid resolution Δx) for the feedback region, and compute the ratio of the mass M_{snr} within this region to the expected shell formation mass $M_{\text{sf}} = 1679 M_{\odot} (n_{\text{H}}/\text{cm}^{-3})^{-0.26}$ (Kim & Ostriker 2015a). Here, M_{snr} is defined by the sum of the gas mass within the initial SN remnant radius R_{snr} and the ejecta mass $M_{\text{ej}} = 10 M_{\odot}$. If $\mathcal{R}_M \equiv M_{\text{snr}}/M_{\text{sf}} > 1$, we regard that the Sedov-Taylor stage of this SN is unresolved and inject a radial momentum $p_{\text{snr}} = 2.8 \times 10^5 M_{\odot} \text{ km s}^{-1} (n_{\text{H}}/\text{cm}^{-3})^{-0.17}$ that represents the final post-cooling value appropriate for the momentum-conserving stage, as calibrated from resolved numerical simulations (e.g., Kim & Ostriker 2015a; Martizzi et al. 2015; Iffrig & Hannebelle 2015; Walch & Naab 2015). If $0.027 < \mathcal{R}_M < 1$, we regard the SN remnant as being in the Sedov-Taylor phase, and add the SN energy $E_{\text{SN}} = 10^{51} \text{ erg}$ in both thermal ($\sim 72\%$) and kinetic ($\sim 28\%$) forms to the surrounding medium within R_{snr} . If $\mathcal{R}_M < 0.027$, we increase R_{snr} until $\mathcal{R}_M \gtrsim 0.027$ and inject E_{SN} within the increased R_{snr} in both thermal and kinetic forms, as above. When \mathcal{R}_M becomes less than 0.027 even for the prescribed maximum value ($\sim 128 \text{ pc}$) of R_{snr} , we inject E_{SN} in kinetic form only, corresponding to the free expansion of the ejecta.

It turns out that in our simulations, the fraction of SN feedback in the free-expansion, Sedov-Taylor, and momentum-conserving phase are, on average, ~ 13 , 57 , and 30% , respectively, indicating that $\sim 70\%$ of SN feedback is resolved. The fraction of the resolved feedback is slightly higher for unmagnetized and/or weaker-arm models. SNe in the interarm region tend to explode at lower density and $\sim 5\%$ more of the SN events are resolved than those in the arm region. The resolved fraction of SN events is $\sim 30\%$ higher for clusters than runaway stars.

We integrate Equations (2)–(5) using a modified ver-

Table 1
Model Parameters and Selected Simulation Outcomes

Model (1)	\mathcal{F} (2)	β (3)	$\log \Sigma_{\text{SFR}}$ (4)	$\log P_{\text{thm}}/k_B$ (5)	$\log P_{\text{trb}}/k_B$ (6)	$\log \Pi_{\text{mag}}/k_B$ (7)	$\log P_{\text{tot}}/k_B$ (8)
F00B10	0.0	10	-2.56 ± 0.13	3.77 ± 0.08	3.64 ± 0.13	3.94 ± 0.07	4.29 ± 0.03
F10B10	0.1	10	-2.47 ± 0.13	3.74 ± 0.09	3.79 ± 0.08	3.99 ± 0.05	4.34 ± 0.03
F20B10	0.2	10	-2.38 ± 0.20	3.75 ± 0.13	3.89 ± 0.11	3.95 ± 0.10	4.36 ± 0.05
F00Binf	0.0	∞	-2.27 ± 0.19	3.85 ± 0.13	3.91 ± 0.12	—	4.19 ± 0.12
F10Binf	0.1	∞	-2.31 ± 0.17	3.78 ± 0.15	3.88 ± 0.14	—	4.15 ± 0.11
F20Binf	0.2	∞	-2.20 ± 0.11	3.80 ± 0.09	4.01 ± 0.14	—	4.22 ± 0.10

Note. — Column 1: model name. Column 2: arm strength. Column 3: plasma parameter. Column 4: logarithm of the SFR surface density ($\text{M}_\odot \text{pc}^{-2} \text{Myr}^{-1}$). Columns 5-8: logarithm of the midplane thermal, turbulent, magnetic, and total stresses over k_B , respectively ($\text{cm}^{-3} \text{K}$). Quantities in Columns 4-8 are averaged over the simulation domain and $t = 200\text{--}600 \text{ Myr}$.

sion of the **Athena** code that utilizes a directionally unsplit Godunov scheme to solve the ideal MHD equations, including the constrained transport algorithm to preserve $\nabla \cdot \mathbf{B} = 0$ within machine precision (Stone et al. 2008). For hydrodynamic variables, we employ shearing-sheet boundary conditions in the horizontal direction (Hawley et al. 1995) and outflow (diode-like) boundary conditions in the vertical direction. The Poisson equation (Equation (6)) is solved based on the FFT method with shearing-sheet boundary conditions in the horizontal direction (e.g., Gammie 2001) and vacuum boundary conditions in the vertical direction (Koyama & Ostriker 2009).

Appendix A presents the equations of motion that sink/star particles obey in the local spiral-arm coordinates. We integrate Equation (A9) using a “kick-drift-kick” scheme for a symplectic integrator suggested by Quinn et al. (2010), with the time t in the last term of Equation (A9a) set equal to t_m for each particle. By applying the shearing-sheet boundary conditions in the horizontal plane (e.g., Huber & Pfenniger 2001; Kim & Ostriker 2007), we ensure that particles leaving the simulation domain from one x -face reenter with shifted y -positions through the opposite x -face.

2.3. Model Parameters

The simulation domain is centered on a location corresponding to a distance $R_0 = 8 \text{ kpc}$ from the galactic center, rotating with angular speed of $\Omega_0 = 30 \text{ km s}^{-1} \text{ kpc}^{-1}$. Our simulation domain has a size of $L_x = \pi \text{ kpc}$ and $L_y = L_z = 2L_x$. The domain is resolved by $256 \times 512 \times 512$ cells, corresponding to a physical size $\Delta x = 12.3 \text{ pc}$, which is marginally good enough to obtain converged results for statistical properties such as SFR, velocity dispersions, scale heights, etc. (Kim & Ostriker 2017). For models that include spiral-arm forcing, we take the pattern speed $\Omega_p = \Omega_0/2$, pitch angle $\sin i = 0.125$, and the arm number $m = 2$.

For all models, the initial surface density is spatially uniform and equal to $\Sigma_0 = 13 \text{ M}_\odot \text{pc}^{-2}$. To specify Φ_* and Φ_{dm} in Equations (7) and (8), we adopt the solar neighborhood values of $\Sigma_* = 42 \text{ M}_\odot \text{pc}^{-2}$, $z_* = 245 \text{ pc}$, and $\rho_{\text{dm}} = 6.4 \times 10^{-3} \text{ M}_\odot \text{pc}^{-3}$ from Kuijken & Gilmore (1989).

Two key dimensionless parameters that characterize

our models are

$$\mathcal{F} \equiv \frac{m}{\sin i} \left(\frac{|\Phi_{\text{arm}}(0)|}{R_0^2 \Omega_0^2} \right), \quad (12)$$

$$\beta \equiv \frac{8\pi P_0}{B_0^2}, \quad (13)$$

where $P_0(z)$ is the initial pressure profile (see below) and $\mathbf{B}_0 = B_0(z)\hat{\mathbf{y}}$ is the initial magnetic field profile, threading the gas parallel to the spiral arm. The \mathcal{F} parameter represents the ratio of the radial force due to the spiral arm to the mean radial gravitational force (Roberts 1969), while the plasma parameter β measures the (inverse of) magnetic pressure relative to the initial thermal pressure. To study the effect of the arm strength and magnetic fields on the gas evolution and star formation, we run six models that differ in the combination of \mathcal{F} and β .

Table 1 lists the model parameters and some of the simulation results. Models with $\beta = 10$ have $B_0(0) = 2.6 \mu\text{G}$ initially at the midplane. For models with a spiral arm ($\mathcal{F} \neq 0$), we turn on the arm potential slowly and make it achieve the full strength at $t = 200 \text{ Myr}$. All simulations are run until $t = 700 \text{ Myr}$.

Initially, the disks are vertically stratified with density $\rho_0(z)$. For $\rho_0(z)$, we take a double exponential

$$\begin{aligned} \rho_0(z) &= \rho_1(z) + \rho_2(z) \\ &= \rho_{10} e^{-\Phi_{0,\text{tot}}/\sigma_1^2} + \rho_{10} e^{-\Phi_{0,\text{tot}}/\sigma_2^2}, \end{aligned} \quad (14)$$

where $\Phi_{0,\text{tot}}(z) = \Phi_*(z) + \Phi_{\text{dm}}(z) + 2\pi G \Sigma_0 |z|$ is the total gravitational potential under the assumption that the gaseous disk is razor-thin (without spiral-arm forcing). With $\rho_{10} = 2.85 m_{\text{H}} \text{ cm}^{-3}$, $\rho_{20} = 10^{-5} \rho_{10}$, $\sigma_1 = 7 \text{ km s}^{-1}$, and $\sigma_2 = 10\sigma_1$, ρ_1 and ρ_2 in Equation (14) represents the warm and hot media, respectively, of the ISM in the Milky Way. We set the initial pressure profile to $P_0(z) = \sigma_1^2 \rho_1 + \sigma_2^2 \rho_2$.

Our initial disks described above are initially out of thermal equilibrium, so that they would instantly experience cooling and heating. The cold gas would collapse toward the midplane and form a thin dense layer and undergo an extreme burst of star formation. To prevent this spurious collapse and star formation, we initially generate pseudo-star particles that survive only for an initial 40 Myr span, which stir the disk by injecting SN feedback similarly to the feedback particles. The creation rate of the pseudo-star particles is set to the value equivalent to the SFR surface density of

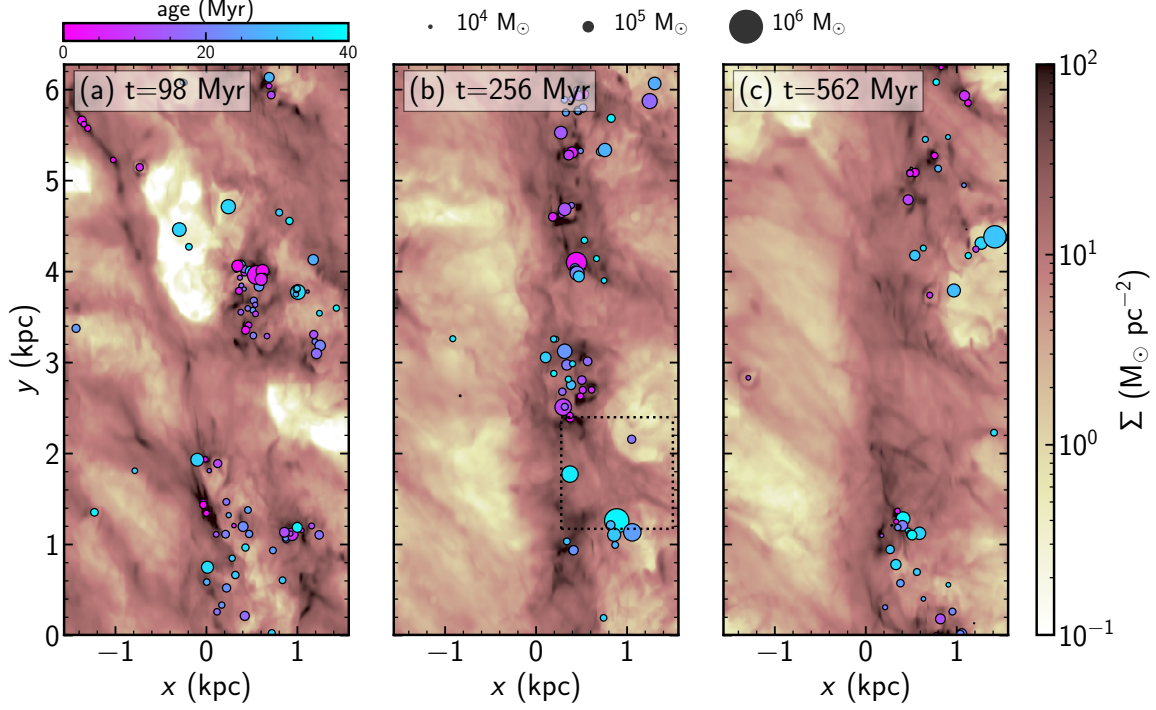


Figure 1. Snapshots of the gas surface density of model F20B10 at (a) $t = 98$ Myr, (b) $t = 256$ Myr, and (c) $t = 562$ Myr. Star particles younger than 40 Myr are projected onto the x - y plane. The color and size of the circles indicate the age and mass of the star particles, respectively. The spiral potential builds up a dense ridge of gas near the potential minimum where most star formation takes place. SN feedback compresses the gas downstream, forming gaseous spurs jutting out perpendicularly from the arm. The squared section in (b) is zoomed in Figure 9 to display the configurations of velocity and magnetic fields around a spur.

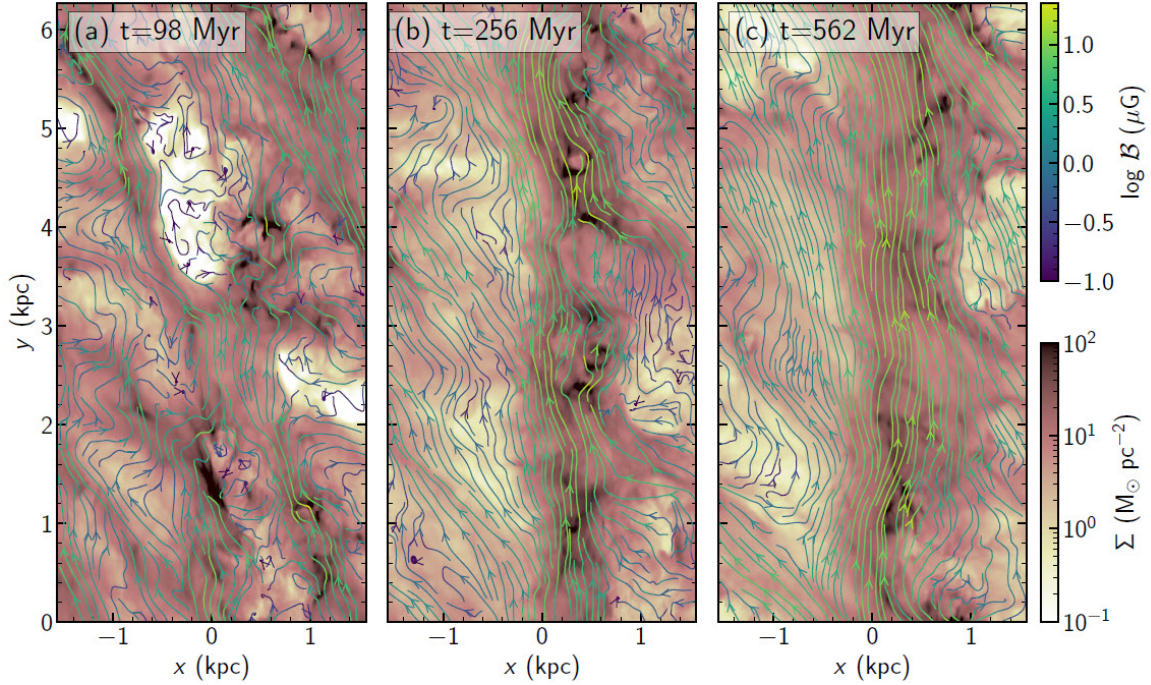


Figure 2. Streamline plots of the vertically-integrated magnetic fields $B_x = \int \rho B_x dz / \Sigma$ and $B_y = \int \rho B_y dz / \Sigma$ overlaid on the gas surface density Σ of model F20B10 at (a) $t = 98$ Myr, (b) $t = 256$ Myr, and (c) $t = 562$ Myr. The color of the streamlines corresponds to logarithm of the strength $B = (B_x^2 + B_y^2)^{1/2}$. Overall, the magnetic fields are parallel to the arm and stronger in the arm than interarm region.

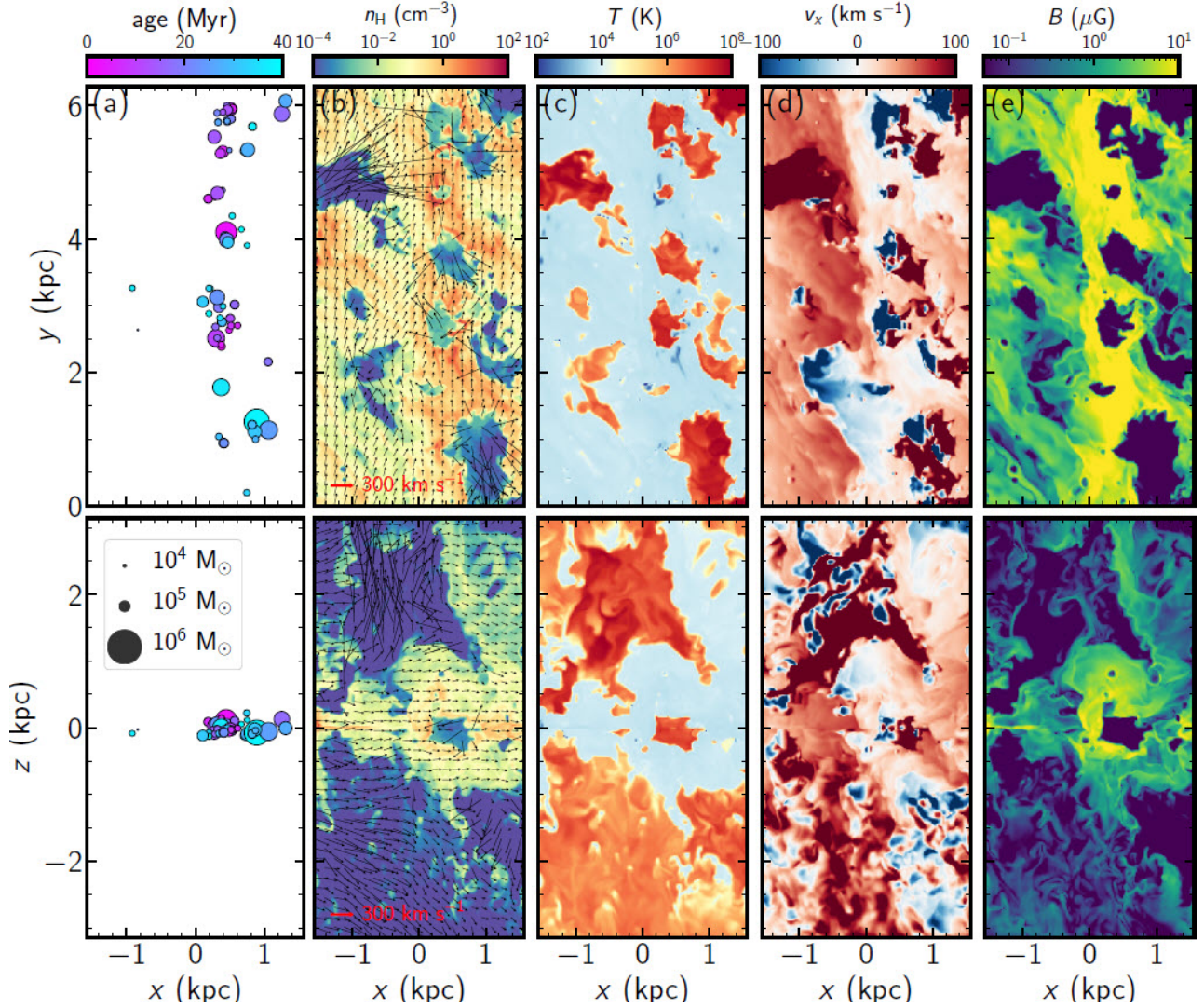


Figure 3. Snapshots at $t = 256$ Myr of model F20B10. The top row panels show slices through the midplane, $z = 0$, and the bottom row panels show vertical slices that cut through the disk perpendicular to the spiral arm at $y = 3.7$ kpc. Individual panels show (a) projected positions of sink/star particles, (b) gas number density n_{H} together with velocity vectors (v_x, v_y) in the top panel and (v_x, v_z) in the bottom panel, (c) temperature T , (d) velocity v_x perpendicular to the arm, and (e) magnetic field strength B . In (a), only the sink/star particles with age younger than 40 Myr are shown, with their color and size representing age and mass, respectively. In (b), the amplitudes of the velocity vectors are indicated as the red arrows.

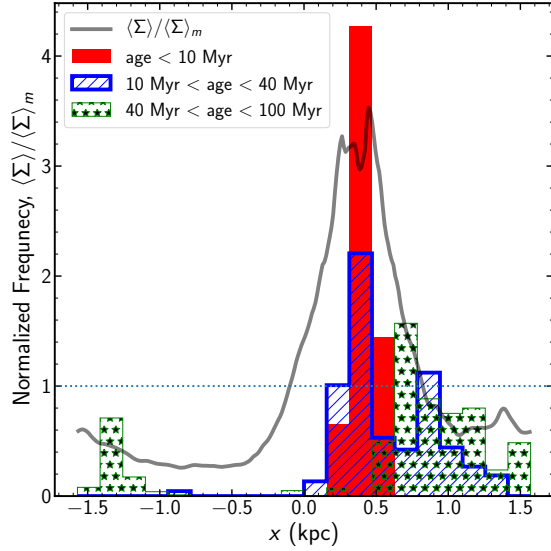


Figure 4. Normalized histograms of the mass-weighted positions of star particles in the x -direction with ages $t_m < 10$ Myr (red filled), $10 \text{ Myr} < t_m < 40$ Myr (blue hatched), and $40 \text{ Myr} < t_m < 100$ Myr (green stars) in model F20B10 at $t = 256$ Myr. For reference we show the normalized surface density $\langle \Sigma \rangle / \langle \Sigma \rangle_m$ averaged along the y -direction plotted as a grey solid line. The horizontal dotted line indicates $\langle \Sigma \rangle / \langle \Sigma \rangle_m = 1$. The youngest cohort of stars coincides with the peak gas surface density of the arm.

$\Sigma_{\text{SFR}} = 5 \times 10^{-3} \text{ M}_{\odot} \text{ pc}^{-2} \text{ Myr}^{-1}$, approximately the quasi-steady value of the solar-neighborhood model in the absence of a spiral arm (Kim & Ostriker 2017). The pseudo-star particle initial locations are chosen randomly in the horizontal direction and follow an exponential distribution in the vertical direction with scale height of 10 pc. These particles are initially assigned background shearing velocity \mathbf{v}_0 as well as random velocities with a one-dimensional dispersion of 10 km s^{-1} .

3. EVOLUTION

In this section, we focus on the temporal and morphological changes of gaseous structures that form due to spiral compression and star formation feedback. Physical quantities averaged over space and time and their correlations will be presented in Section 4.

3.1. Overall Evolution of the Fiducial Model

We first describe evolution of our fiducial model F20B10 with $\mathcal{F} = 0.2$ and $\beta = 10$. Figure 1 plots snapshots of the gas surface density $\Sigma = \int \rho dz$, together with the projected distributions of young star particles in the x - y plane, at a few selected epoches in model F20B10. Figure 2 displays streamline plots of the vertically-integrated in-plane magnetic fields $(\mathcal{B}_x, \mathcal{B}_y) = \int \rho(B_x, B_y) dz / \Sigma$ overlaid on the surface density distribution at the same epoches as in Figure 1. Figure 3 plots the distribution of sink/star particles younger than 40 Myr, gas number density n_{H} , temperature T , velocity v_x perpendicular to the arm, and magnetic field strength $B = |\mathbf{B}|$ in the (top) $z = 0$ and (bottom) $y = 3.7$ kpc plane of model F20B10 at $t = 256$ Myr when the spiral potential is strong and star formation is active.

Pseudo-star particles introduced initially provide density and velocity perturbations to the gaseous medium that would otherwise be uniform in the x - y plane. Due

to the background shear and self-gravity, the perturbations rotate kinematically with time and are amplified as they swing from leading to trailing configurations (e.g., Kim & Ostriker 2001). Dense trailing filaments tend to have stronger magnetic fields than the surrounding underdense regions. In addition to swing amplification, some filaments become denser and colder as they collide with neighbors. Filaments that achieve sufficient density undergo gravitational collapse and spawn star particles (Figure 1a). Newly created star particles heat up cold gas to the warm phase. Subsequent SN feedback creates hot gas bounded by expanding shells of the cold/warm gas around the star particles.² Supershells created by clustered SNe expand to ~ 1 kpc in diameter before being distorted significantly by the background shear or undergoing collisions with neighboring shells. Collisions of expanding, shearing shells produce high-density clumps susceptible to new star formation. Since the strength of the spiral potential is growing slowly, the early phase ($t \lesssim 100$ Myr) of evolution is similar to that of the TIGRESS run without spiral structure presented in Kim & Ostriker (2017).

As the strength of the spiral potential increases further, material is preferentially gathered toward the potential minimum. These converging motions of the gas inevitably result in the formation of a dense ridge of gas located at $x \sim 0.2$ kpc roughly parallel to the y -direction, which occurs at $t \sim 162$ Myr in model F20B10. Magnetic fields are overall parallel to the ridge and stronger in the regions with larger gas density, while being slightly inclined in the interarm region (Figure 2). The arm density is naturally inhomogeneous along its length due to collisions of shearing filaments and shells. It is in the high-density regions along the ridge where most star formation takes place, although some clusters also form in downstream gaseous spurs after they develop.

Star formation is usually clustered, as indicated by the distributions of star particles shown in Figure 1(b). Clustered star formation forms superbubbles filled with weakly-magnetized, rarefied hot gas bounded by strongly-magnetized, dense shells (Figure 3). Strong SN feedback from the star particles expels the gas away from the star-forming sites. Gas motions induced by feedback are limited, however, by the high-density ridge slightly to the right (downstream) from the potential minimum. Gas pushed by feedback toward the upstream side of the galaxy rotation collides with the gas that is flowing into the arm, reinforcing the high-density ridge. Large-scale spiral shocks produced by these gas collisions, as delineated by sharp discontinuities of v_x at $x \sim -0.6$ – 0 kpc, are evident in Figure 3(d). Apparently, the shock fronts are not straight in the y -direction and consist of numerous small-scale curved shocks. The shocked gas is soon pushed back by the ram pressure of the interarm gas toward the potential minimum, suggesting that the spiral shocks oscillate with large amplitudes along the x -direction. On the other hand, gas pushed downstream by supernova explosions can easily leave the arm region,

² Following the convention of Kim & Ostriker (2017), we classify the gas into five phases according to its temperature: cold ($T < 184$ K), unstable ($184 \text{ K} < T < 5050$ K), warm ($5050 \text{ K} < T < 2 \times 10^4$ K), ionized ($2 \times 10^4 \text{ K} < T < 5 \times 10^5$ K), and hot ($T > 5 \times 10^5$ K).

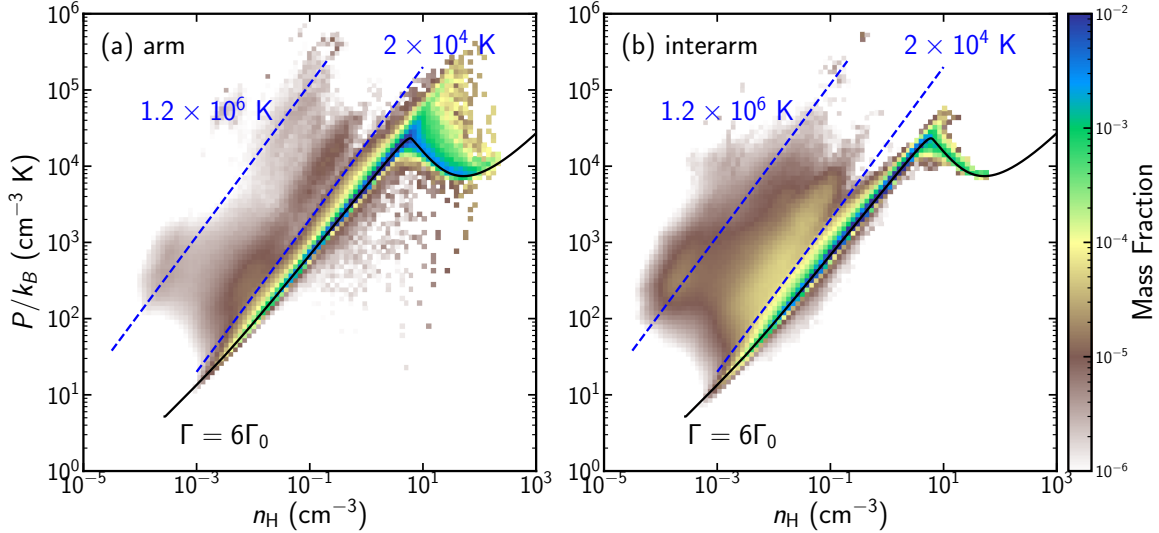


Figure 5. Instantaneous distribution in the density-pressure plane of the gas in (a) the arm region at $-0.1 \text{ kpc} < x < 0.8 \text{ kpc}$ and (b) the interarm region at $x < -0.1 \text{ kpc}$ or $x > 0.8 \text{ kpc}$ of model F20B10 at $t = 256 \text{ Myr}$. The color represents the mass fraction of the gas. In each panel, the black solid line draws the thermal equilibrium curve for instantaneous heating rate $6\Gamma_0$, while blue dashed lines indicate the minimum ($2 \times 10^4 \text{ K}$) and mean ($1.2 \times 10^6 \text{ K}$) temperatures of the ionized-hot phase.

supplying the interarm region.

New star particles produced in the arm climb out of the arm potential well as they follow their epicycle orbits downstream (see Appendix A). They inject SN feedback in both arm and interarm regions. The mean speed of star particles perpendicular to the arm is $v_{0x} \sim 15 \text{ km s}^{-1}$, so that the SN feedback is concentrated mostly in a zone within $\sim v_{0x}t_{\text{life}} = 0.6 \text{ kpc}$ from the star-forming sites. Feedback from spatially uncorrelated star particles tends to simply increase random velocity dispersions of the surrounding gas.

The boundaries of distorted superbubbles typically take the form of dense structures attached to the arm in the surface density maps, as shown in Figure 1. Due to the velocity acquired during the superbubble expansion, swept-up gas in the midplane moves in positive or negative y -direction, with velocities $\sim 20\text{--}30 \text{ km s}^{-1}$ relative to the local background. Relatively weak filaments are quickly swept/washed out by expansions of newly created bubbles nearby. Filaments strong enough to survive interactions with small bubbles undergo a collision with neighboring one, forming even denser, longer structures that extend almost over the whole length of the interarm region. Figure 1(b) displays three large-scale gas structures located at $y \sim 1.6, 4.0$, and 5.7 kpc , with the peak surface densities of $\sim 15, 22, 20 \text{ M}_\odot \text{ pc}^{-2}$ measured at $x = 1 \text{ kpc}$, respectively. Such large-scale structures may be observed as gas and dust spurs/feathers in real spiral galaxies. In our simulations, strong spurs can produce star formation at their densest parts usually close to the arm, but sometimes deep in the interarm region.

Since star particles form mostly in the dense ridge and age as they move downstream, one can naturally expect an age gradient along the direction perpendicular to the arm. Figure 4 plots the normalized histograms of the mass-weighted x -positions of star particles with age $t_m < 10 \text{ Myr}$ (red filled), $10 \text{ Myr} < t_m < 40 \text{ Myr}$ (blue hatched), and $40 \text{ Myr} < t_m < 100 \text{ Myr}$ (green stars) in model F20B10 at $t = 256 \text{ Myr}$. For comparison, we also plot the y -averaged surface density $\langle \Sigma \rangle = \int \Sigma dy / L_y$ nor-

malized to the mean value $\langle \Sigma \rangle_m \equiv \int \langle \Sigma \rangle dx / L_x$ as a grey solid line. As expected, younger star particles tend to be crowded closer to the density peak located at $x \sim 0.3\text{--}0.5 \text{ kpc}$: the mass-weighted mean locations of the star particles with $t_m < 10 \text{ Myr}$, $10 \text{ Myr} < t_m < 40 \text{ Myr}$, and $40 \text{ Myr} < t_m < 100 \text{ Myr}$ are at $x_m = 0.42, 0.59$, and 1.1 kpc , respectively, with the standard deviations of $\sigma(x_m) = 0.47, 0.87, 1.4 \text{ kpc}$, respectively.³ These correspond roughly to $dx_m/dt_m \sim 10 \text{ pc Myr}^{-1}$ and $d\sigma(x_m)/dt_m \sim 14 \text{ pc Myr}^{-1}$ at $t = 256 \text{ Myr}$. When averaged over $t = 200\text{--}600 \text{ Myr}$, we find the mean age gradient $dx_m/dt_m \sim 8.7 \pm 3.9 \text{ pc Myr}^{-1}$ and the dispersion $d\sigma(x_m)/dt_m \sim 15.2 \pm 9.3 \text{ pc Myr}^{-1}$, insensitive to \mathcal{F} and β . This shows that older stars tend to be found farther away from the ridge and spread out more widely than younger stars.

We note, however, that older star particles are not always found downstream from younger star particles. This is because star formation sometimes occurs away from the ridge, and because some particles move in the negative x -direction on their epicycle orbits, mixing particles with different ages.

Based on the mean surface density, we define “arm” and “interarm” regions as the regions with $\langle \Sigma \rangle / \langle \Sigma \rangle_m$ greater or smaller than unity, respectively (cf. Fig. 4). In model F20B10, the arm region is at $-0.1 \text{ kpc} < x < 0.8 \text{ kpc}$, varying slightly with time, and the rest of the domain is regarded as the interarm region.

Figure 5 plots the mass-weighted probability distribution functions (PDFs) in the pressure–density plane for the gas in the (a) arm and (b) interarm regions at $t = 256 \text{ Myr}$ of model F20B10. Two dashed diagonal lines mark the minimum ($2 \times 10^4 \text{ K}$) and mean ($1.2 \times 10^6 \text{ K}$) temperatures for the ionized-hot phase. At this time, the majority of the gas is close to the instantaneous thermal equilibrium curve indicated by the black solid line

³ In calculating x_m and $\sigma(x_m)$, we add L_x to the x -coordinate for the star particles located at $x < 0$, consistent with the periodic boundary condition.

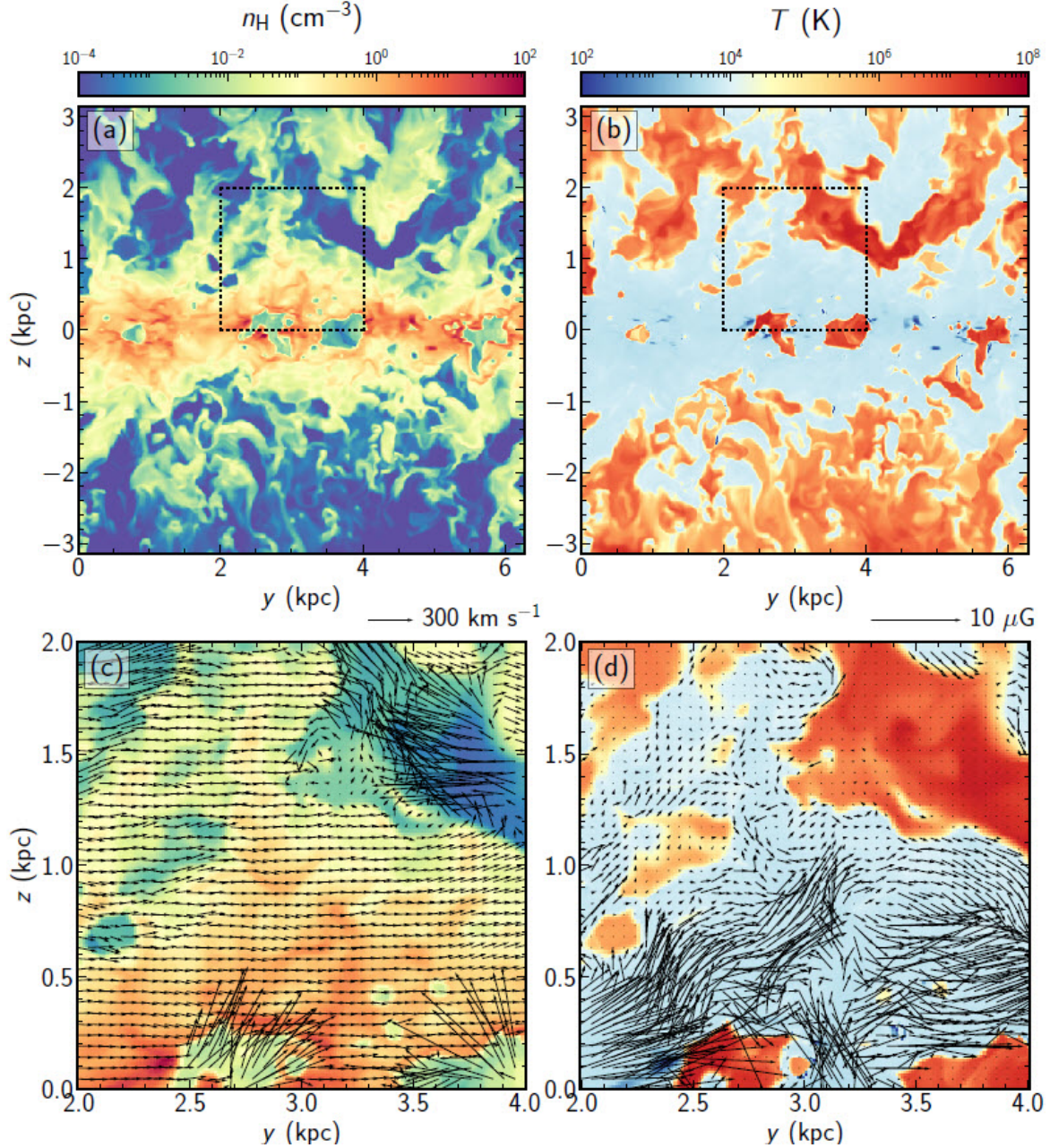


Figure 6. Distributions of (a) gas density and (b) gas temperature for model F20B10 at $t = 256$ Myr. Both panels represent vertical slices that cut through the center of the spiral arm at $x = 0.45$ kpc. The section marked by a dotted square in the upper panels is enlarged in the lower panels to overlay the velocity vectors (v_y, v_z) in (c) and the magnetic field vectors (B_y, B_z) in (d). The arrows above in (c) and (d) measure the amplitudes of velocity and magnetic-field vectors, respectively.

with $\Gamma = 6\Gamma_0$.

Including gas at all heights, the mass fractions of the cold-unstable, warm, and ionized-hot phases in the arm region are 0.16, 0.83, and 7.7×10^{-3} , respectively, which change to 2.6×10^{-2} , 0.95, 2.4×10^{-2} in the interarm region. The corresponding volume fractions of the cold-unstable, warm, and ionized-hot phases are 2.6×10^{-3} , 0.44, and 0.56 in the arm, and 8.7×10^{-4} , 0.30, and 0.70 in the interarm region, respectively. For gas within $|z| \leq 1$ kpc, the volume fraction of the warm phase is increased to 0.78 and 0.50 in the arm and interarm regions, respectively. For gas at the midplane, the area fractions of the warm and ionized-hot phases are 0.71 and 0.26 in the arm, and 0.74 and 0.25 in the interarm regions,

respectively. This indicates that gas in both arm and interarm regions is predominantly in the warm phase by mass (also by volume near the midplane), and most of the cold gas is in the arm region. Due to the deeper gravitational potential, the gas in the arm region tends to be denser and colder, and has higher pressure to support its weight against gravity, than in the interarm region.

Cold and warm gas is lifted to high- $|z|$ regions from the midplane due to the vertical momenta of superbubbles which drift with the background flows as they expand. Figure 6 plots the y - z distributions of the gas density and temperature at $x = 0.45$ kpc of model F20B10 at $t = 256$ Myr in the upper panels as well as their zoomed-in views together with velocity and mag-

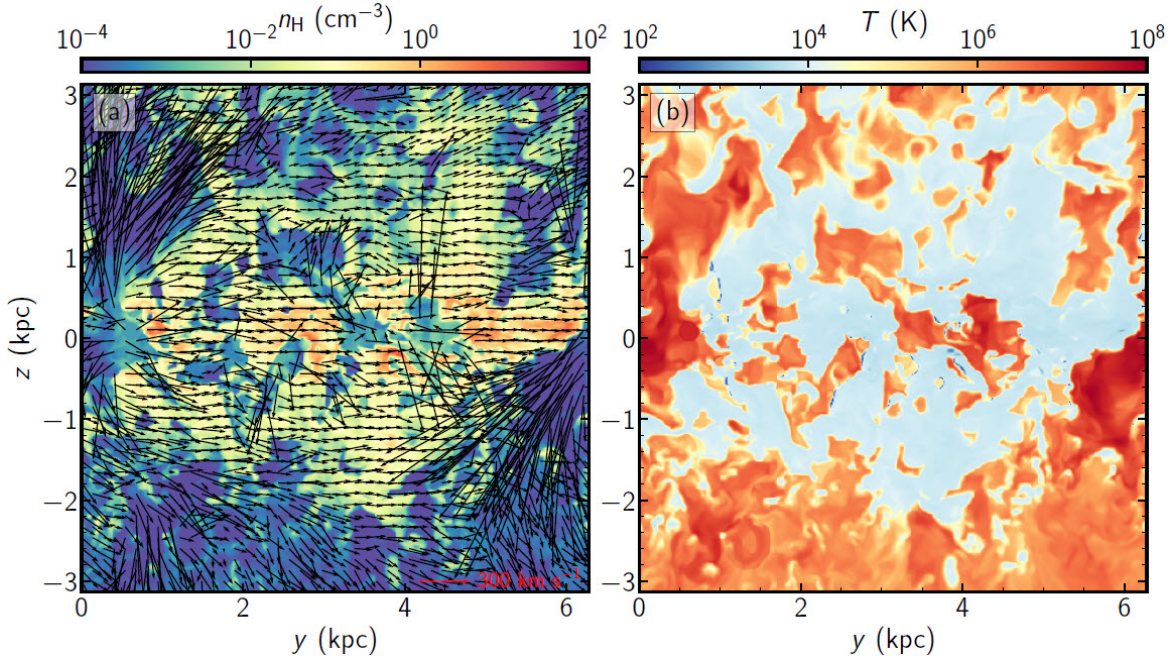


Figure 7. Distributions of (a) gas density and (b) gas temperature for model F20B10 at $t = 235$ Myr at $x = 0.90$ kpc, downstream from the density peak of the spiral arm. Hot gas is vented to high- $|z|$ regions through chimneys located near $(y, z) = (0.5, 1)$ kpc and $(6, -0.5)$ kpc. The red arrow at the bottom of (a) measures the amplitudes of velocity vectors.

netic field structures in the lower panels. Apparently, the gas distribution near the midplane in spiral arms is highly clumpy, characterized by expanding low-density bubbles surrounded by distorted high-density shells. Expansion speeds of hot gas in superbubbles easily exceed the speed of galaxy rotation, pushing on the surrounding dense shell to drive turbulence in the warm ISM. Expanding superbubbles transport the midplane gas to high- $|z|$, causing the height of the regions with largest density (hence highest SFR) to occur at $|z| \sim 40$ pc rather than at $z = 0$ (see below).

Superbubbles usually break out from the cold-warm midplane layer in the interarm region downstream from the densest region of the arm, leading to the rise of hot gas to high- $|z|$ regions. Figure 7 plots a slice through the density and temperature distributions in the y - z plane at $x = 0.90$ kpc for model F20B10 at $t = 235$ Myr. A superbubble centered at $(y, z) = (0.5 \text{ kpc}, 0)$ breaks out vertically and produces two slightly inclined chimneys through which hot, tenuous gas is vented to high- $|z|$ regions. Because of our periodicity in y , the vent towards positive z appears at small y and the vent towards negative z appears mostly at large y in the figure. As previously discussed by Kim & Ostriker (2018), superbubbles can drive warm gas to large $|z| \sim 1 - 3$ kpc. Since this warm gas does not achieve the escape velocity ($\sim 200 \text{ km s}^{-1}$), it falls back toward the midplane, creating a warm galactic fountain. In contrast, the hot gas in chimneys has high velocities, and in our simulations is lost through the vertical boundaries located at $z = \pm\pi$ kpc. In real galaxies, this venting produces a hot galactic wind.

Supernova/superbubble shell expansions, mutual collisions, and interactions with the background shear and gravitational potential drive turbulent motions in the gas. While SN feedback is concentrated primarily in zones immediately downstream from star-forming re-

gions, the injected energies and momenta are advected by the mean flows to make all of the gas turbulent across the simulation domain. The related gas motions also stretch, twist, and amplify magnetic fields that tend to be strong in high-density regions. Figure 6(d) shows that although magnetic fields point on average in the y -direction (i.e., parallel to the spiral arm), they change their directions quite rapidly in the y - z plane, indicating that the turbulent component of magnetic fields is as strong as the regular component. We defer more detailed discussion of the magnetic fields to Section 4.4.

After the spiral potential is fully turned on, the system reaches a quasi-steady state in the sense that feedback from star formation in the arm region drives turbulence and heating that balance dissipation and radiative losses of turbulent and thermal energies. Still, Figure 1 shows that the spiral arm at $t = 562$ Myr is less concentrated, harbors less active star formation, and is associated with less pronounced spurs, compared to the arm at $t = 256$ Myr. This is caused primarily by the secular reduction in the gas mass over time in our simulations. With no gas inflow from outside, continued star formation as well as mass loss at the vertical boundaries keep decreasing the gas mass over time. Reduced self-gravity further lowers the gas density and hence SFR in the arm region.

3.2. Other Models

The evolution in models with no spiral potential is similar to that of the “Solar neighborhood” TIGRESS run presented in Kim & Ostriker (2017), in that most star formation takes place in sheared filaments distributed across the simulation domain. There is neither formation of dense ridges resembling spiral arms nor gaseous spurs perpendicular to the arms. In contrast, models with a spiral potential all form dense arm ridges and gaseous spurs, regardless of the presence of magnetic fields, sim-

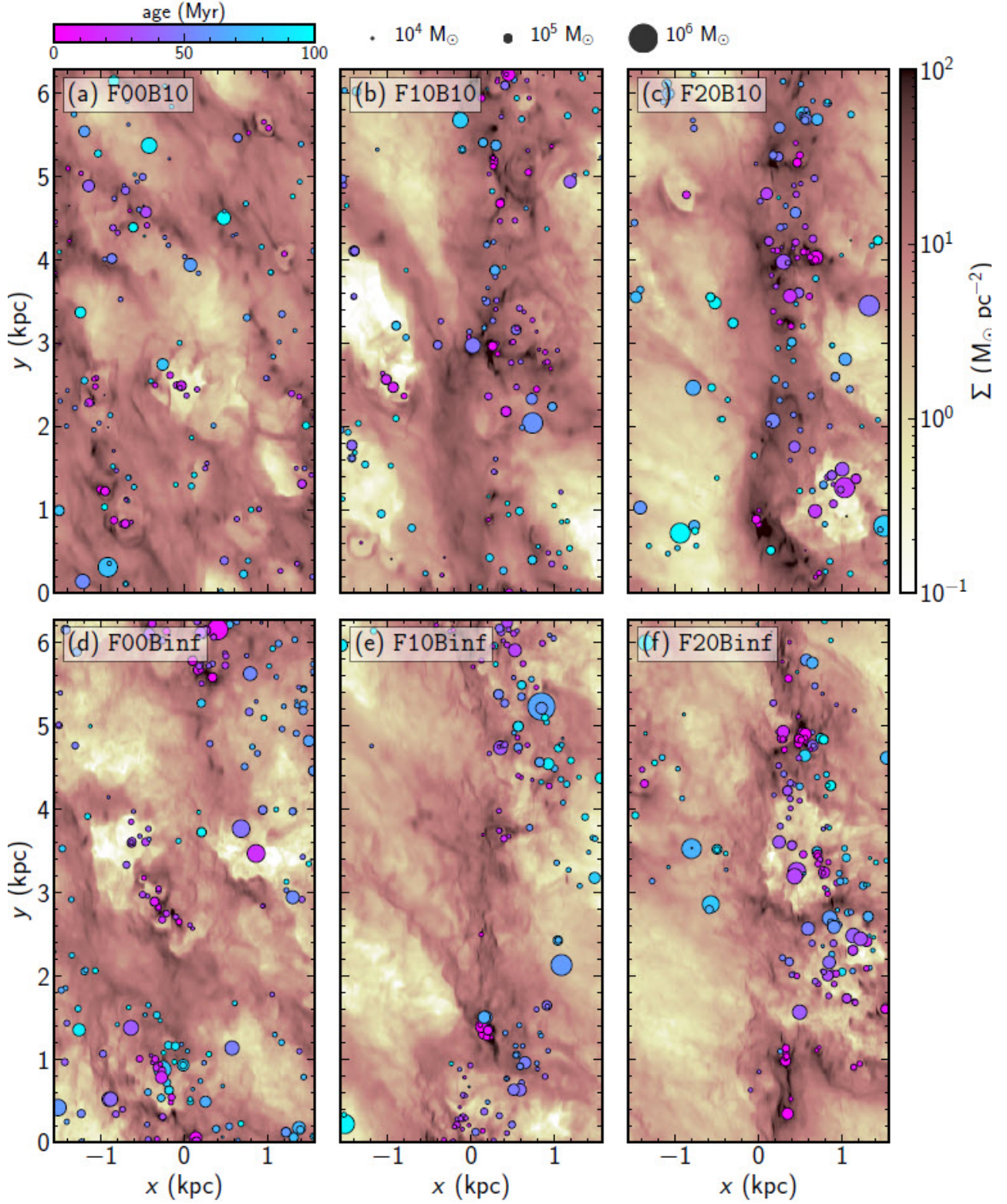


Figure 8. Snapshots of gas surface density at $t = 300$ Myr for the (top) magnetized and (bottom) unmagnetized models. Star particles younger than 100 Myr are overlaid as circles, with their color and size denoting the age and mass, respectively. In models without spiral potential (left column), star formation occurs in shearing filaments distributed across the simulation domain. In the models with $\mathcal{F} = 0.1$ (middle column), the spiral potential produces a star-forming, dense ridge parallel to the arm, and interarm spurs. In the models with $\mathcal{F} = 0.2$ (right column), dense ridges and spurs are more pronounced than in the $\mathcal{F} = 0.1$ counterpart.

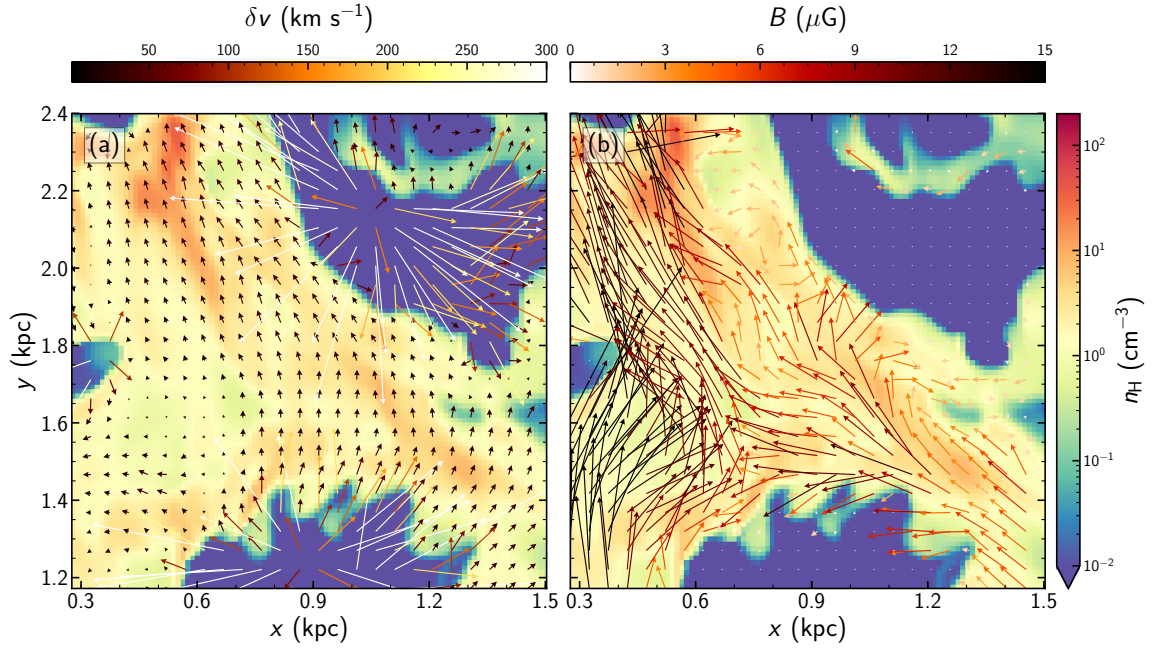


Figure 9. Zoomed-in view of the spur in the region marked by a square in Figure 1(b), from model B10F20 at $t = 256$ Myr. Vector fields of the perturbed velocity $(\delta v_x, \delta v_y) \equiv (v_x - v_{0x}, v_y - v_{0y})$ and the magnetic field (B_x, B_y) are overlaid on the midplane gas number density (color scale). The color (and length) of the vectors represents the amplitude of (a) the in-plane perturbed velocity $\delta v = (\delta v_x^2 + \delta v_y^2)^{1/2}$ and (b) the in-plane magnetic field $B = (B_x^2 + B_y^2)^{1/2}$. The spur is confined by two superbubbles centered at $(x, y) = (0.9, 1.2)$ kpc and $(1.1, 2.1)$ kpc. Magnetic fields are parallel to the arm at $x \lesssim 0.7$ kpc, and to the spur at $x \gtrsim 0.7$ kpc.

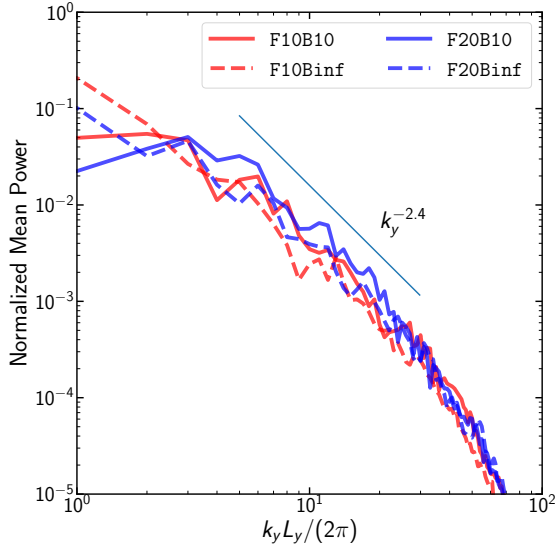


Figure 10. Mean power spectra of the integrated surface density $\int_{0.8 \text{ kpc}}^{1.2 \text{ kpc}} \Sigma(x, y, t) dx$ averaged over $200 \text{ Myr} \leq t \leq 300 \text{ Myr}$ as a function of the dimensionless wavenumber $n_y = k_y L_y / (2\pi)$ for models with a spiral arm. Each power spectrum is normalized to unity at $n_y = 0$. The short line segment draws the slope of -2.4 , which best describes the surface-density power in the range with $5 \leq n_y \leq 30$.

ilarly to the fiducial model. The ridge density and the number of spurs depends on \mathcal{F} and β .

Figure 8 plots the distributions of the gas surface density in the x - y plane for all models at $t = 300 \text{ Myr}$. Star particles with age less than 100 Myr are overlaid as circles. While star particles are widely distributed in models without a spiral potential (left column), they are concentrated along the dense ridges in models with spiral potential (middle and right columns). Note that all models with $\mathcal{F} \neq 0$ possess spurs that jut out approximately perpendicularly from the arm and turn to trailing configurations in the interarm region. Weaker spiral-arm forcing in model F10B10 produces a less pronounced ridge and induces more distributed star formation in the x -direction compared to model F20B10. Without magnetic support, star formation in unmagnetized models is more active, which in turn makes the ridges less dense and broader in the x -direction compared to the magnetized counterpart.

3.3. Spur/Feather Formation

As mentioned above, gaseous spurs/feathers form in both magnetized and unmagnetized models as long as the spiral potential is present. To illustrate the structure of large-scale spurs formed in our simulations, Figure 9 enlarges the square sector marked in Figure 1(b) and plots the in-plane velocity and magnetic fields overlaid on the gas density in the $z = 0$ plane. Clearly, the spur at $y \sim 1.6 \text{ kpc}$ is bounded by the SN feedback regions created by two groups of star particles located at $(x, y) = (0.9, 1.2) \text{ kpc}$ and $(1.1, 2.1) \text{ kpc}$. The material in the spur moves roughly parallel to the arm with velocities $\delta v_y = v_y - v_{0y} \sim 30 \text{ km s}^{-1}$ relative to the background flows. In the arm region, magnetic fields have strength $\sim 10\text{--}14 \mu\text{G}$, and are oriented overall parallel to the arm. In the interarm region, on the other hand, compression by the expanding superbubbles orients magnetic fields so

that they approximately follow the direction of the spurs (see also Figure 2), with strength $\sim 4\text{--}8 \mu\text{G}$. The lifetime of feedback-induced spurs is rather short, of order of $\sim 30 \text{ Myr}$. After cessation of the correlated feedback that created a given spur structure, its destruction is accomplished primarily by feedback from neighboring regions (and sometimes the spur itself).

Large-scale spurs in our simulations are created by the collisions of sheared supershells that in turn form due to clustered star formation in the arm region. This implies that the presence of spurs requires strong star formation in the arm and spatially correlated feedback. Our fiducial model possesses prominent spurs mostly during the period $200 \text{ Myr} \lesssim t \lesssim 300 \text{ Myr}$ when the spiral potential is fully turned on and the arm has a plenty of gas available for active star formation. To estimate the typical spur spacing in our simulations, we calculate the mean surface density averaged over a narrow strip with $x \in [0.8, 1.2] \text{ kpc}$ where spurs are strong, and take its Fourier transform along the y -direction. Figure 10 plots the mean power spectra averaged over $t = 200\text{--}300 \text{ Myr}$ as a function of the dimensionless y -wavenumber $n_y = k_y L_y / (2\pi)$, normalized to unity at $n_y = 0$, for models with a spiral potential. The power spectra in models F10B10 and F20B10 are dominated by the modes with $n_y = 2$ and 3 , corresponding to two and three spurs, respectively, while $n_y = 1$ and 2 modes are significant in models F10Binf and F20Binf. This indicates that the typical spur spacing in our magnetized simulations is $\sim 2\text{--}3 \text{ kpc}$, with the smaller value corresponding to a stronger arm. In all models, the power spectra have a slope of -2.4 over $n_y \in [5, 30]$, which is slightly shallower than the two-dimensional (2D) Kolmogorov spectrum with a slope of $-8/3$.

With reduction in the arm gas density, star formation at $t \gtrsim 300 \text{ Myr}$ becomes distributed and spatially uncorrelated, and the associated feedback occurs almost randomly in the y -direction. Bubbles and shells that form are usually small (less than $\sim 0.5 \text{ kpc}$) in size, and collide with each other to create small filaments, some of which undergo star formation in the interarm region. We note that arm star formation can still be clustered and correlated, but this occurs relatively rarely during the late time evolution of our simulations. When highly clustered star formation events do occur at late times, they are followed by formation of large-scale spurs.

Finally, we note that smaller-scale spurs can form temporarily as some of the material collected into “superclouds” in the arm moves out into the interarm region, where it is sheared out into trailing filaments. This process is somewhat reminiscent of the spur-formation mechanism originally identified by Kim & Ostriker (2002). There, self-gravitating perturbations grew in the dense, magnetized arm regions, with the overdensities advected into the interarm region then forming spurs. In those earlier models, the only physical source driving large-scale perturbations was self gravity (aided by magnetic stresses). In contrast, when correlated supernovae are present as in the current work, they are able to drive large-scale velocity flows that create (and also destroy) spiral arm spurs.

4. TEMPORAL AND SPATIAL VARIATIONS OF PHYSICAL QUANTITIES

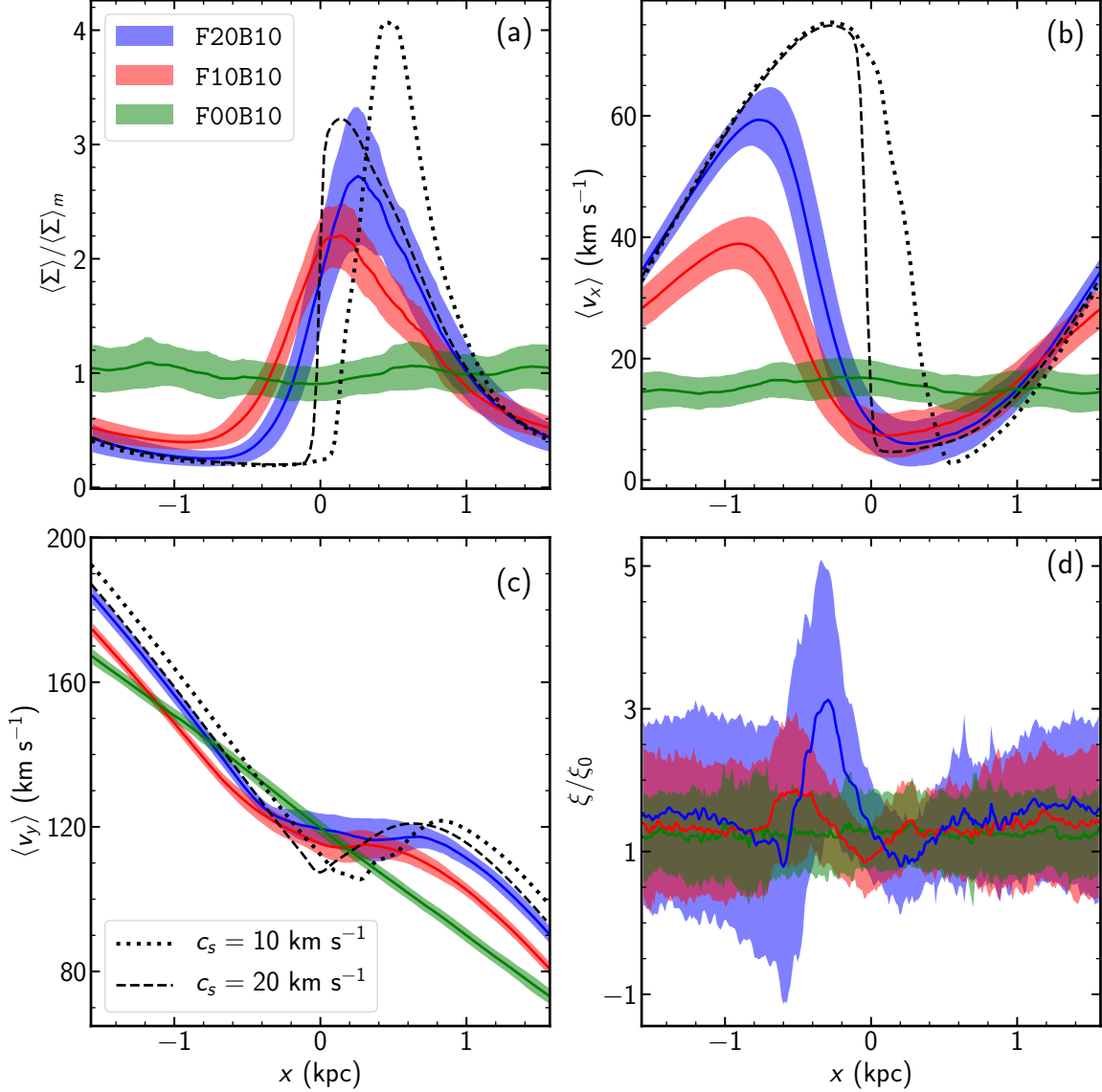


Figure 11. Profiles perpendicular to the arm of (a) normalized surface density $\langle \Sigma \rangle / \langle \Sigma \rangle_m$, (b) velocity perpendicular to the arm $\langle v_x \rangle$, (c) velocity parallel to the arm $\langle v_y \rangle$, and (d) normalized PV ξ / ξ_0 . All magnetized models are shown, with \mathcal{F} for each model indicated in the key. The solid lines give the (y -averaged) mean values over $t = 200-600$ Myr, while the shades indicate the standard deviations. For reference, the dotted and dashed lines in (a)–(c) plot the arm profiles in a vertically-stratified, isothermal disk without star formation, with a sound speed $c_s = 10$ and 20 km s $^{-1}$, respectively, and other parameters as in model F20B10.

We now investigate the profiles of various physical quantities such as surface densities, velocities, SFR, magnetic fields etc., as well as correlations among them. For these profiles, the independent variable is the quasi-radial coordinate, i.e., the distance perpendicular to the spiral arm. We also present the temporal evolution of volume-integrated quantities including the SFR and mass fractions.

4.1. Spiral Arm Profiles

It is interesting to compare the averaged arm profiles from our simulations with the much simpler case of isothermal spiral shocks without star formation (theory for the latter dates back to Roberts 1969).⁴ Figure 11 plots for the magnetized models the depen-

dence on x of (a) the normalized gas surface density $\langle \Sigma \rangle / \langle \Sigma \rangle_m$, (b) the density-weighted quasi-radial velocity $\langle v_x \rangle \equiv \int \rho v_x dy dz / \int \rho dy dz$, (c) the density-weighted quasi-azimuthal velocity $\langle v_y \rangle \equiv \int \rho v_y dy dz / \int \rho dy dz$, and (d) the normalized PV $\xi \equiv (d\langle v_y \rangle / dx + 2\Omega_0) / \langle \Sigma \rangle$ relative to the initial value $\xi_0 = (2 - q)\Omega_0 / \Sigma_0 \rightarrow \Omega_0 / \Sigma_0$ (e.g., Balbus 1988; Kim & Ostriker 2002, 2006). The solid lines draw the temporal averages over $t = 200-600$ Myr, while the shades represent the standard deviations. For comparison, we also plot examples of profiles in x for quasi-steady solutions in the isothermal case, including self-gravity (but with no star formation and feedback),

the full velocity $\langle v_y \rangle$ shown in Figure 11(c) is not periodic in x , its perturbed part, $\langle v_y \rangle - v_{0y}$, is periodic. Although the background velocity v_{0y} varies linearly in x (Equation 1), this does not alter the form of the perturbation equations that control the (linear or nonlinear) arm profile (see also Shu et al. 1973; Kim et al. 2014).

⁴ Roberts (1969) took a quasi-axisymmetric approximation to obtain one-dimensional periodic solutions of spiral shocks. While

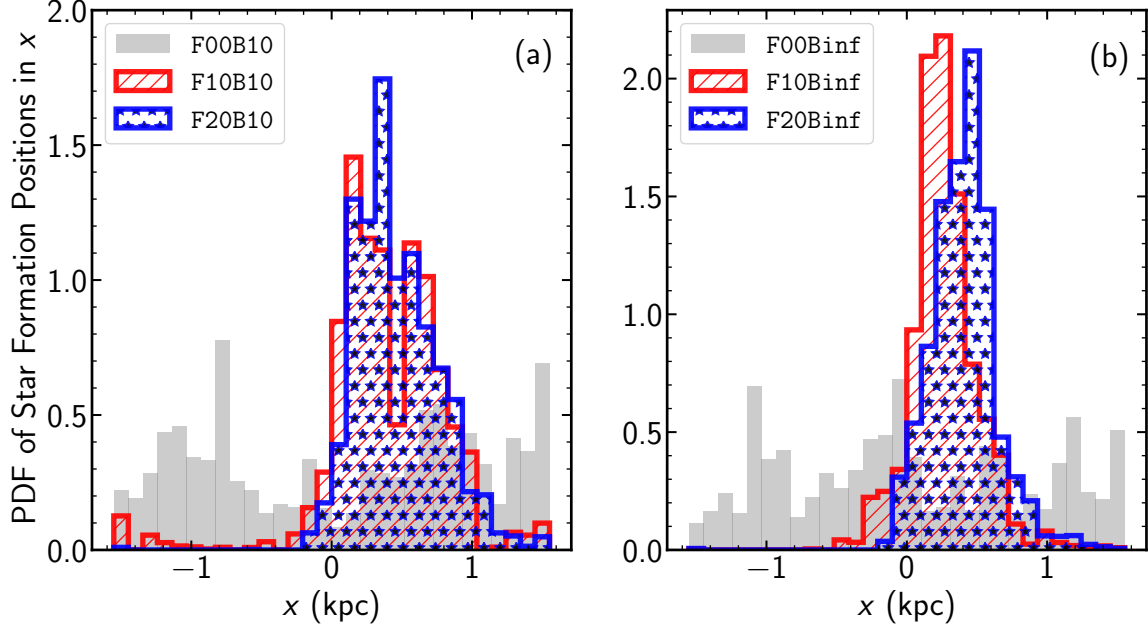


Figure 12. PDFs of the mass-weighted positions of star-forming regions in the x -direction over $t = 200\text{--}600$ Myr for (a) magnetized and (b) unmagnetized models.

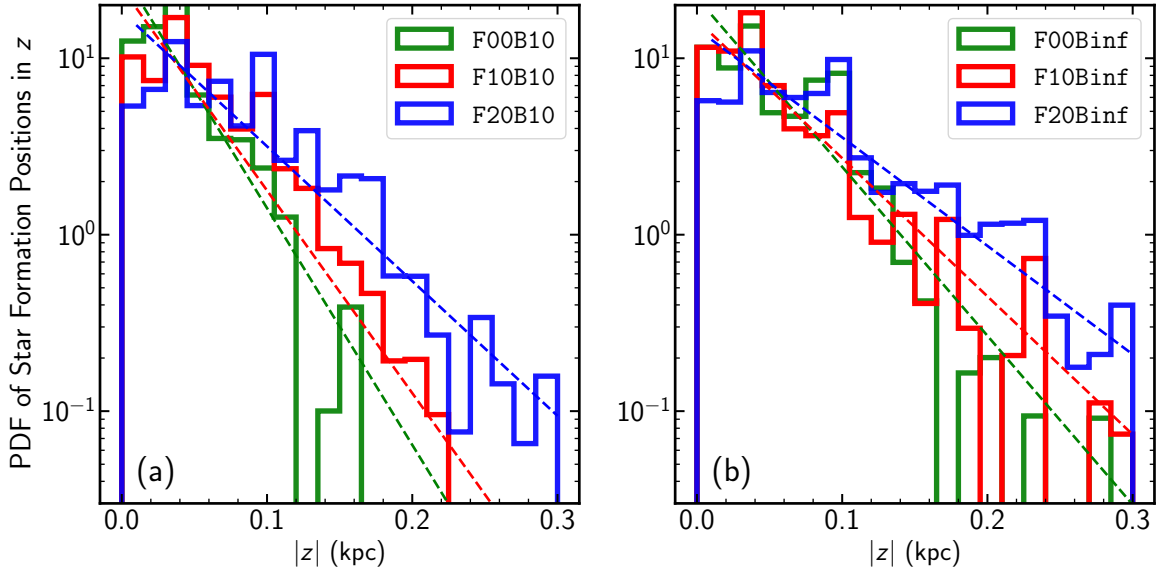


Figure 13. PDFs of the mass-weighted positions of star-forming regions in the z -direction over $t = 200\text{--}600$ Myr for (a) magnetized and (b) unmagnetized models. The dashed lines are fits to the PDFs. See text for details.

based on a vertical average of an $x - z$ spiral shock solution. The cases shown as black dotted and dashed lines have sound speed $c_s = 10$ and 20 km s^{-1} , respectively, with the other arm and disk parameters set equal to those of model F20B10.

In model F00B10 with no arm, the averaged profiles are very close to their initial distributions. The mean PV is enhanced by about $\sim 20\%$ most likely due to vorticity generation across numerous curved shocks produced by SN feedback. Also, the presence of magnetic fields contributes to the changes of PV (e.g., Webb & Mace 2015).

In models with spiral arms, the spiral potential compresses the gas toward the potential minimum, increasing (decreasing) gas surface density in the arm (interarm) region. For a steady flow that varies only with x , mass flux

Σv_x and PV ξ are conserved, which leads to the characteristic profiles shown for the isothermal models: (1) with the rapid increase of Σ moving into the shock, v_x rapidly decreases, while in the post-shock and interarm region where $\langle \Sigma \rangle$ steadily decreases, v_x steadily increases; (2) in the arm region where $\Sigma/\Sigma_0 > 2/(2 - q) \rightarrow 2$, the azimuthal shear $dv_y/dx \approx R_0 d\Omega/dR$ becomes positive (e.g., Roberts 1969; Shu et al. 1973; Balbus & Cowie 1985). Simple isothermal models with stronger spiral-arm forcing and lower sound speed also tend to have stronger shocks with density peaks further downstream (e.g., Kim & Ostriker 2002; Kim et al. 2014). Some of these features are recovered in the present (much more physically complex) simulations, while others are not.

Evidently, stronger spiral-arm forcing in the F20B10

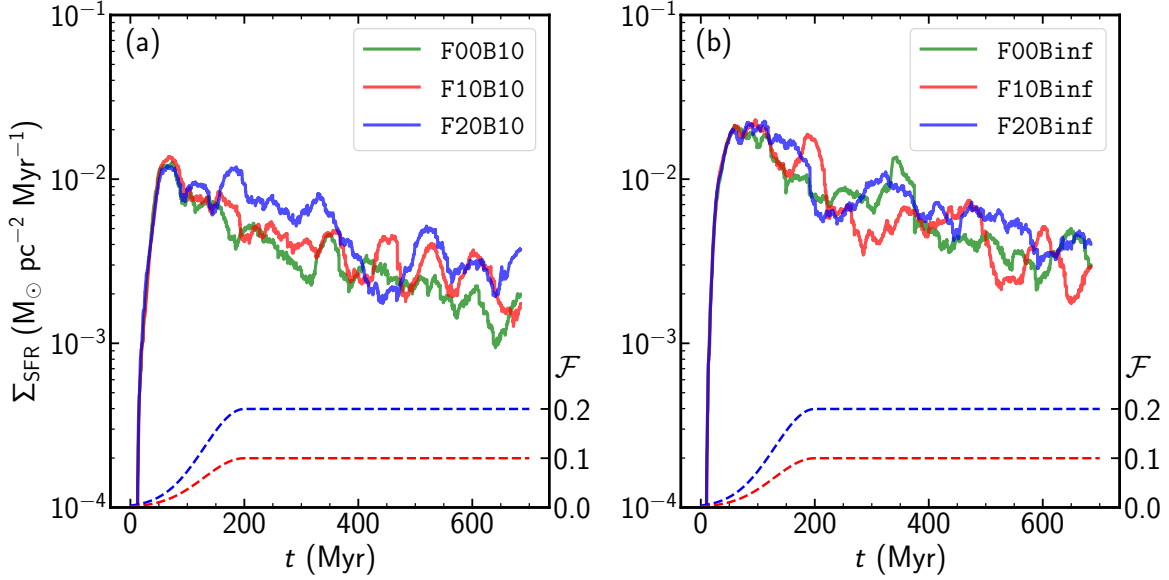


Figure 14. Temporal evolution of the global SFR surface density (solid lines; left axis), Σ_{SFR} , measured using star particles younger than 40 Myr, for (a) magnetized and (b) unmagnetized models. Dashed lines (right axis) plot the time variation of the spiral-arm forcing, \mathcal{F} , in our spiral-arm models. Σ_{SFR} rapidly rises initially, achieves a peak at $t \sim 60\text{--}70$ Myr, and then decreases secularly with time. Unmagnetized models have higher Σ_{SFR} than their magnetized counterparts. The spiral-arm forcing enhances Σ_{SFR} , but by less than a factor 1.6 on average.

model compared to F10B10 does result in larger changes in Σ and v_x , and places the density peak farther downstream. In terms of the peak density and its location, the spiral-arm profiles in model F20B10 are similar to those in the isothermal counterpart with $c_s = 20 \text{ km s}^{-1}$. We find, however, that the oscillations of spiral shocks in the x -direction (both in time and along y) mentioned in Section 3.1 smear out the averaged profiles considerably, especially near $x \sim 0$ where the spiral shocks are found. This smearing makes the y -averaged increase in Σ and decrease in v_x on the upstream side of the arm less steep than the isothermal models. The smearing, in combination with magnetic and Reynolds stresses that break conservation of angular momentum, removes the region of shear reversal (i.e., $dv_y/dx > 0$) that is a characteristic feature of simple, one-dimensional isothermal spiral shocks. Curved shocks along the dense ridges (see Figures 1 and 8) are responsible for the local peak in PV near $x \sim -0.3 \text{ kpc}$ in model F20B10.

4.2. Star Formation

Figures 12 and 13 plot the PDFs of the mass-weighted positions of star formation sites in the x - and z -directions, respectively, during $t = 200\text{--}600$ Myr, for the (a) magnetized and (b) unmagnetized models. Star formation in models with no arm is widely distributed in the x -direction, with large fluctuations due to stochasticity. The spiral potential gathers the star-forming regions close to the arm where the gas is also concentrated. When the arm is defined as the region where the y -averaged gas surface density exceeding the domain-averaged value (see Section 3.1 and Figure 11(a)), for example, $\sim 95\%$ and $\sim 90\%$ of all star formation occurs inside the arm in models F20B10 and F10B10, respectively. The fraction of the arm star formation is increased to $\sim 98\%$ and $\sim 97\%$ in models F20Binf and F10Binf without magnetic fields, respectively. Most of the interarm star formation occurs in strong spurs/feathers.

Figure 13 shows that star formation is concentrated toward the midplane, although the most probable locations are at $|z| \sim 40 \text{ pc}$ rather than at $z = 0$ for all models. The PDFs in $|z|$ are overall described by an exponential function, $\propto \exp(-|z|/H_{\text{SF}})$, with a scale height of $H_{\text{SF}} = 75, 87, 131 \text{ pc}$ in models F00B10, F10B10, F20B10 and $H_{\text{SF}} = 100, 128, 163 \text{ pc}$ in models F00Binf, F10Binf, F20Binf, respectively. Models with stronger arms have higher H_{SF} , and the presence of magnetic fields tends to reduce H_{SF} by about 30%. This is because a higher SFR in the unmagnetized models can lift the dense gas to higher- $|z|$ regions than in the magnetized models. Due to the spiral arm compression, gas in models with higher \mathcal{F} is denser in the arm and can achieve the threshold density for star formation at higher $|z|$.

To define profiles of the star formation rate surface density, Σ_{SFR} , in the direction perpendicular to the arm, at any given time we select young star particles with age less than 40 Myr and bin their x -positions into $n_{\text{bin}} = 15$ partitions with width $w_{\text{bin}} = L_x/n_{\text{bin}} \simeq 0.21 \text{ kpc}$. Let $M_{\text{sp},i}$ denote the total mass of the young star particles in the i -th bin, with integer $i = 1, 2, \dots, n_{\text{bin}}$. At a given time, the local SFR surface density in the i -th bin can then be calculated as

$$\Sigma_{\text{SFR}}(x_i) \equiv \frac{M_{\text{sp},i}}{40 \text{ Myr} \cdot w_{\text{bin}} L_y}, \quad (15)$$

where $x_i = -L_x/2 + (i+0.5)w_{\text{bin}}$. The global SFR surface density across the simulation domain is given by $\Sigma_{\text{SFR}} = n_{\text{bin}}^{-1} \sum_{i=1}^{n_{\text{bin}}} \Sigma_{\text{SFR}}(x_i)$.

Figure 14 plots temporal variations of the global SFR surface density Σ_{SFR} for (a) magnetized and (b) unmagnetized models. For reference we also indicate (dashed lines) the temporal changes of \mathcal{F} in models with spiral-arm forcing. In all models, Σ_{SFR} rapidly increases with time initially, as the system adjusts from its initial transient state. The value of Σ_{SFR} tops out at around $t \sim 60\text{--}70$ Myr, independent of \mathcal{F} and β , when SN feedback and

Table 2

Mass fractions, Velocity Dispersions, and Scale Heights of Various Phases

Model (1)	Phase (2)	$\log f_m$ (3)	$\log \sigma_z$ (4)	$\log H$ (5)
F00B10	total	0	1.05 ± 0.07	2.52 ± 0.03
	cold-unstable	-0.66 ± 0.13	0.72 ± 0.04	1.86 ± 0.05
	warm	-0.12 ± 0.04	1.07 ± 0.05	2.55 ± 0.04
	ionized-hot	-2.26 ± 0.11	1.90 ± 0.08	3.17 ± 0.02
F10B10	total	0	1.12 ± 0.05	2.59 ± 0.04
	cold-unstable	-0.72 ± 0.14	0.84 ± 0.03	2.02 ± 0.06
	warm	-0.10 ± 0.03	1.12 ± 0.04	2.62 ± 0.05
	ionized-hot	-2.23 ± 0.10	1.93 ± 0.08	3.18 ± 0.03
F20B10	total	0	1.16 ± 0.06	2.63 ± 0.04
	cold-unstable	-0.78 ± 0.14	0.92 ± 0.04	2.12 ± 0.07
	warm	-0.09 ± 0.04	1.15 ± 0.05	2.65 ± 0.04
	ionized-hot	-2.15 ± 0.12	1.92 ± 0.07	3.16 ± 0.02
F00Binf	total	0	1.40 ± 0.07	2.80 ± 0.05
	cold-unstable	-0.93 ± 0.14	0.94 ± 0.05	2.02 ± 0.08
	warm	-0.07 ± 0.02	1.31 ± 0.03	2.81 ± 0.05
	ionized-hot	-1.72 ± 0.08	2.08 ± 0.07	3.19 ± 0.02
F10Binf	total	0	1.43 ± 0.06	2.82 ± 0.08
	cold-unstable	-0.97 ± 0.14	1.01 ± 0.07	2.08 ± 0.10
	warm	-0.06 ± 0.02	1.36 ± 0.06	2.83 ± 0.09
	ionized-hot	-1.70 ± 0.12	2.06 ± 0.07	3.18 ± 0.02
F20Binf	total	0	1.44 ± 0.03	2.83 ± 0.07
	cold-unstable	-1.00 ± 0.14	1.08 ± 0.07	2.16 ± 0.09
	warm	-0.06 ± 0.02	1.37 ± 0.05	2.84 ± 0.07
	ionized-hot	-1.71 ± 0.12	2.04 ± 0.06	3.16 ± 0.03

Note. — The mean values and standard deviations are taken over $t = 200\text{--}600$ Myr. Column 3: logarithm of the mass fraction. Column 4: logarithm of the vertical velocity dispersion (km s^{-1}). Column 5: logarithm of the vertical scale height (pc).

radiative heating self-consistently balance turbulence dissipation and cooling. At this time, the spiral forcing shown as the dashed lines remains weak. The peak value of $\Sigma_{\text{SFR}} \sim 1.2 \times 10^{-2} \text{ M}_\odot \text{ pc}^{-2} \text{ Myr}^{-1}$ in the magnetized models (Figure 14a) is similar to Σ_{SFR} in the (magnetized) TIGRESS run of Kim & Ostriker (2017) which has the same surface density, external potential, etc. The peak Σ_{SFR} in magnetized models is about half that of the unmagnetized models shown in Figure 14b, and as expected the overall Σ_{SFR} is higher for unmagnetized models than their magnetized counterparts (see Kim & Ostriker 2015b). Subsequently, in all models Σ_{SFR} exhibits a secular decay as well as large-amplitude quasi-periodic variations with period ~ 50 Myr. The secular decay is caused by the decrease in the gas mass in the simulation domain (see below), while the quasi-periodic fluctuations reflect self-regulation cycles of star formation: SN feedback and heating puff up the disk vertically and thus reduce the SFR; lower feedback in turn cools down the disks and promotes a new round of star formation and feedback (Kim & Ostriker 2017).

Inclusion of the spiral potential enhances Σ_{SFR} , but the effect is relatively modest overall, and at some times Σ_{SFR} can even be larger in models without a spiral potential. Column 4 of Table 1 lists the mean SFR surface density and its standard deviation averaged over $200 \text{ Myr} \leq t \leq 600 \text{ Myr}$ for all models. The mean SFR of model F20B10 is larger, but only by a factor of 1.6, compared to model F00B10. The SFR enhancement factor is reduced to 1.2 in the unmagnetized models. This suggests that triggering of star formation by spiral arms is only moderate and the main effect of arms is rather to collect star-forming regions into narrow ridges.

The very weak dependence of Σ_{SFR} on \mathcal{F} is, of course, due to the regulation of star formation by radiative heating and SN feedback: strong star formation in the arm is accompanied by correspondingly strong feedback that temporarily reduces the SFR by injecting energy and momentum, leading to $\Sigma_{\text{SFR}} \propto \Sigma$ for a fixed external gravity (see below; see also Ostriker et al. 2010; Ostriker & Shetty 2011). This is more significant in the unmagnetized models where stronger feedback makes the arm gas more turbulent and thus less prone to the spiral-arm forcing.

Equation (15) gives $\Sigma_{\text{SFR}}(x_i)$ at any given time, and for each radial position bin x_i we can compute a histogram of these values. The top panels of Figure 15 plots these histograms over $t = 200\text{--}600$ Myr for the magnetized models. In the lower panels of Figure 15, we show histograms of the corresponding gas depletion times $\tau_{\text{dep}}(x_i) = M_{\text{gas},i} / [w_{\text{bin}} L_y \Sigma_{\text{SFR}}(x_i)]$ as a function of x_i . Here, $M_{\text{gas},i} = L_y \int_{x_i - w_{\text{bin}}/2}^{x_i + w_{\text{bin}}/2} \langle \Sigma \rangle dx$ is the gas mass in the i -th bin. The solid lines draw the median values (excluding points with zero Σ_{SFR} or infinite τ_{dep}), while the color represents frequency of occurrence. The corresponding distributions for the unmagnetized models (not shown) are qualitatively similar, although they have, on average, twice larger Σ_{SFR} and three times smaller τ_{dep} than the magnetized counterparts. In model F00B10 with no arm, $\Sigma_{\text{SFR}}(x) \sim 2 \times 10^{-3} \text{ M}_\odot \text{ pc}^{-2} \text{ Myr}^{-1}$ and $\tau_{\text{dep}}(x) \sim 4.7 \text{ Gyr}$, roughly constant in x . In model F20B10, star formation is concentrated in the arm with a rate $\Sigma_{\text{SFR}} \gtrsim 10^{-2} \text{ M}_\odot \text{ pc}^{-2} \text{ Myr}^{-1}$, which is more than an order of magnitude larger than in the interarm region where star formation is scarce. Correspondingly, the median value of the gas depletion time is $\sim 1 \text{ Gyr}$ in the arm, about an order of magnitude shorter than in the interarm region.

Comparison of Figures 11 and 15 shows that the SFR is higher in regions with higher density. To describe the relationship between the SFR surface density and the gas surface density based on profiles, we bin $\langle \Sigma \rangle$ into $n_{\text{bin}} = 15$ partitions to calculate the local mean density $\langle \Sigma \rangle_i = w_{\text{bin}}^{-1} \int_{x_i - w_{\text{bin}}/2}^{x_i + w_{\text{bin}}/2} \langle \Sigma \rangle dx$ in the i -th bin. Figure 16 plots 2D histograms of $\Sigma_{\text{SFR}}(x_i)$ and $\langle \Sigma \rangle_i$ for all spiral-arm models over $t = 200\text{--}600$ Myr, analogous to a Schmidt-Kennicutt plot (Schmidt 1959; Kennicutt 1989, 1998). Since the current models have only a single value of Σ_0 and since averaging along y reduces large excursions in $\langle \Sigma \rangle_i$ relative to the mean (while simultaneously increasing scatter in $\Sigma_{\text{SFR}}(x_i)$), the ranges of Σ_{SFR} and $\langle \Sigma \rangle$ are quite narrow in each of our simulations. Therefore, we have combined all the data from models with spiral-arm forcing. Despite the large scatter, there is a rough correlation between $\Sigma_{\text{SFR}}(x_i)$ and $\langle \Sigma \rangle_i$. The dashed line is our best fit:

$$\Sigma_{\text{SFR}}(x_i) = 4.61 \times 10^{-3} \text{ M}_\odot \text{ pc}^{-2} \text{ Myr}^{-1} \left(\frac{\langle \Sigma \rangle_i}{10 \text{ M}_\odot \text{ pc}^{-2}} \right)^{1.19}, \quad (16)$$

for models with $\mathcal{F} \neq 0$. We remark that Equation (16) is based on y -averaged binning approach that can encompass quite diverse conditions, resulting in a lot of scatter.

4.3. Mass Fractions, Velocity Dispersion, and Scale Height

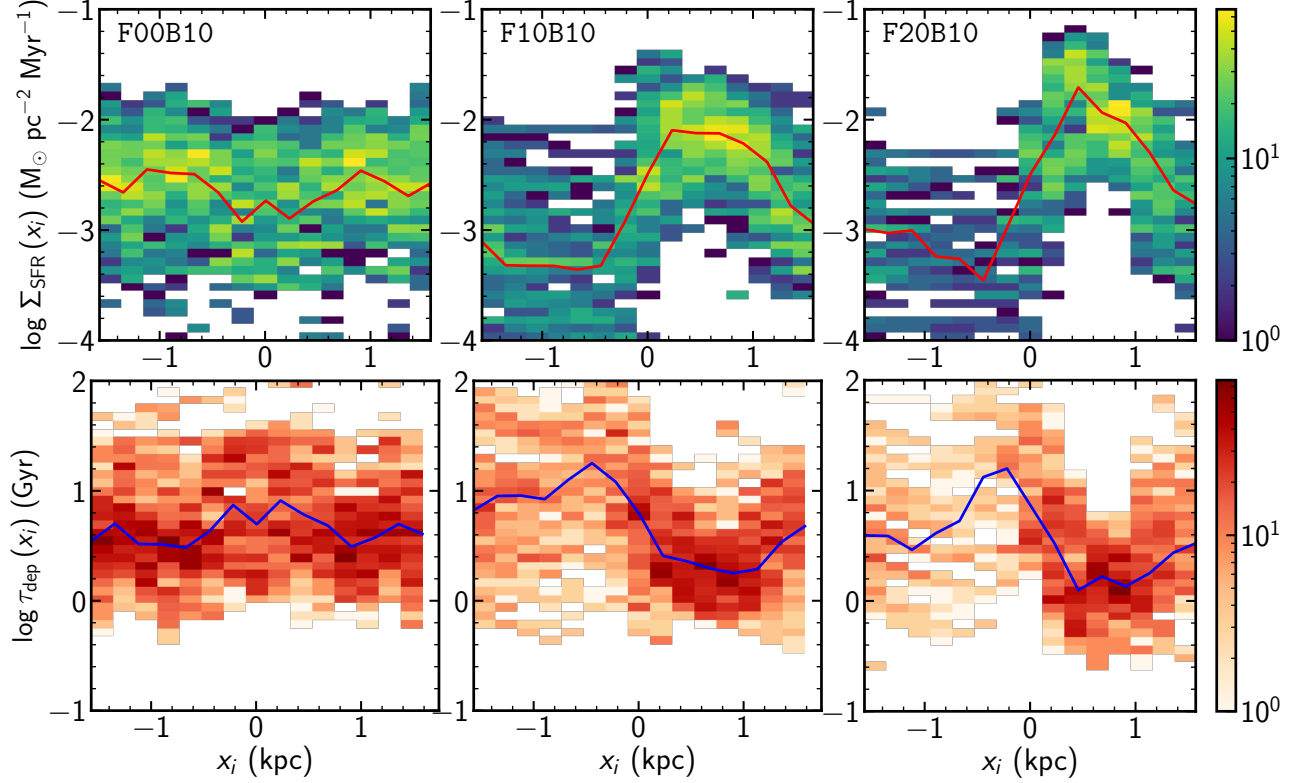


Figure 15. Histograms over $t = 200\text{--}600$ Myr of (top) the local SFR surface density Σ_{SFR} and (bottom) the gas depletion time τ_{dep} for (left) model F00B10, (middle) model F10B10, and (right) model F20B10. The colorbars represent frequency of occurrence. The solid lines draw the median values. Star formation rates are based on star particles younger than 40 Myr.

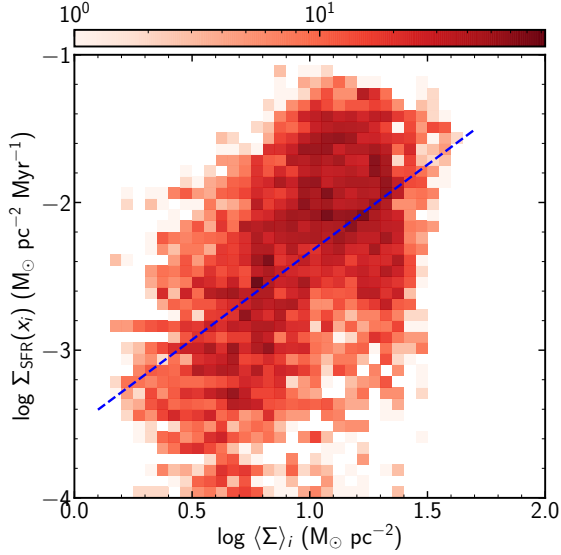


Figure 16. 2D histogram of the local SFR surface density $\Sigma_{\text{SFR}}(x_i)$ and the local surface density $\langle \Sigma \rangle_i$ over $t = 200\text{--}600$ Myr for all models with spiral-arm forcing ($\mathcal{F} \neq 0$). The dashed line draws the best fit, Equation (16).

Figure 17 plots temporal changes of the mass fractions in gas (thin solid) and star particles (thick solid) in the simulation domain together with the fraction of the gas lost through the vertical boundaries (dotted), relative to the initial gas mass, for the (a) magnetized and (b) unmagnetized models. Due to the larger SFRs, the increase in the stellar mass and the lost gas mass is larger in the unmagnetized models. The effect of the spiral potential

is insignificant (tens of percent) compared to the effect of the magnetic field (factor of two). For instance, model F20Binf has converted 46% of its initial gas mass to stars at $t = 700$ Myr, which is only 13% larger than in model F00Binf. In comparison, the respective stellar conversion proportions at the same time are 29% and 21% for models F20B10 and F00B10. The amount of the mass lost in the unmagnetized models is $\sim 20\text{--}30\%$, which is decreased to $\sim 5\%$ in the magnetized models. Model F10Binf experiences massive mass loss around $t \sim 200\text{--}220$ Myr, which is caused by an explosive star formation event occurred at $t \sim 190$ Myr.

Figure 18 plots temporal evolution of key properties of the ISM gas, separated by thermal phase. We show the mass fractions f_m , the density-weighted vertical velocity dispersions σ_z , and the density-weighted scale heights H of the gas in different phases for (left) magnetized and (right) unmagnetized models. Here, σ_z and H of each phase are calculated as

$$\sigma_z = \left(\frac{\int \rho v_z^2 \Theta(T) dx dy dz}{\int \rho \Theta(T) dx dy dz} \right)^{1/2}, \quad (17)$$

$$H = \left(\frac{\int \rho z^2 \Theta(T) dx dy dz}{\int \rho \Theta(T) dx dy dz} \right)^{1/2},$$

where $\Theta(T)$ is an on/off function such that $\Theta = 1$ if the gas temperature is within the range of the phase, and $\Theta = 0$ otherwise. All quantities reach roughly a quasi-steady state after $t = 100$ Myr, although they all fluctuate and a few quantities show modest secular changes associated with the decrease in the gas mass and SFR.

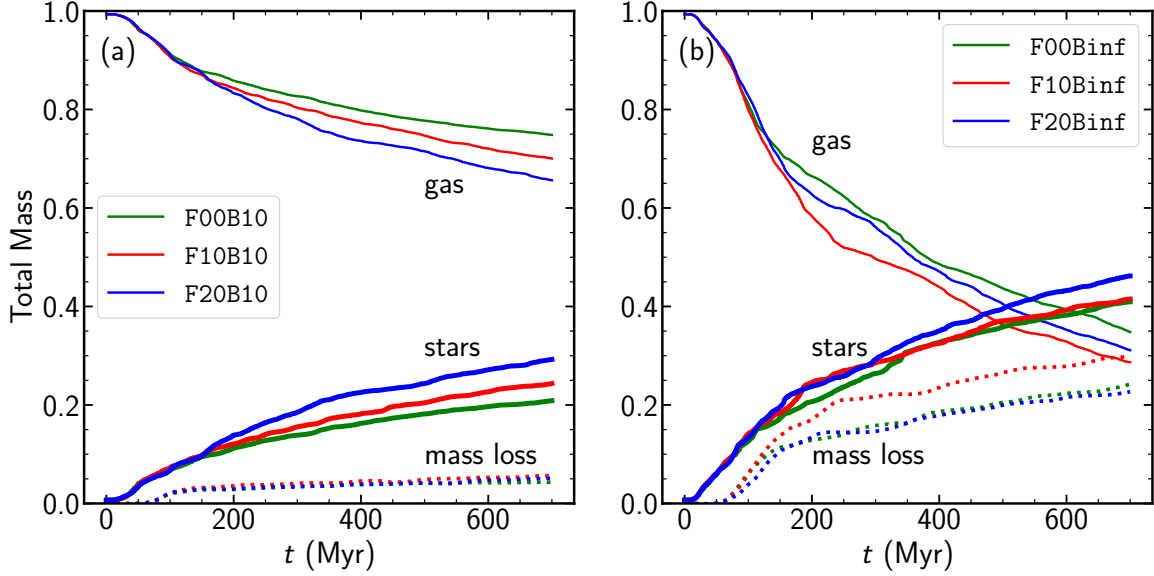


Figure 17. Temporal evolution of the mass fractions of gas (thin solid), star particles (thick solid), and gas lost as outflows through the vertical boundaries (dotted) for (a) magnetized and (b) unmagnetized models.

In all models, most of the gas mass is in the warm phase. The unmagnetized models have less cold-unstable phase and more ionized-hot phase than the magnetized model due to more active star formation. The unmagnetized models also have larger velocity dispersions and scale heights for all phases. Overall, the vertical velocity dispersion and the scale height are smallest ($\sigma_z \sim 10 \text{ km s}^{-1}$ and $H \sim 0.1 \text{ kpc}$) for the cold-unstable phase and largest ($\sigma_z \sim 100 \text{ km s}^{-1}$ and $H \sim 1.5 \text{ kpc}$) for the ionized-hot phase. Table 2 lists the time-averaged values and standard deviations over $t = 200\text{--}600 \text{ Myr}$ for the mass fractions, vertical velocity dispersions, and scale heights of each phase, as well as the total gas.

4.4. Magnetic Fields

As Figures 2, 6, and 9 show, magnetic fields in our simulations possess a regular component as well as an irregular, turbulent component. Following Kim & Ostriker (2015b), we define the y -average of a physical quantity q as

$$\bar{q}(x, z) \equiv \int q dy / L_y, \quad (18)$$

and calculate the regular field $\bar{\mathbf{B}}(x, z)$ and turbulent field $\delta\mathbf{B} \equiv \mathbf{B} - \bar{\mathbf{B}}$. The density-weighted regular, turbulent, and total components in the $j (= x, y, z)$ direction are then calculated as

$$B_{\text{reg},j}(x) = \frac{\int \bar{\rho} \bar{B}_j dz}{\int \bar{\rho} dz}, \quad (19a)$$

$$B_{\text{trb},j}(x) = \frac{\int \overline{\bar{\rho} \delta B_j^2}^{1/2} dz}{\int \bar{\rho} dz}, \quad (19b)$$

$$B_{\text{tot},j}(x) = \frac{\int \bar{\rho} \bar{B}_j^2 dz}{\int \bar{\rho} dz}, \quad (19c)$$

respectively. Note that $\bar{B}_j^2 = \bar{B}_j^2 + \overline{\delta B_j^2}$ by definition. If the magnetic fields change their directions rapidly in

space, $|\mathbf{B}_{\text{reg}}|$ would underestimate the total strength significantly.

Figure 19(a) plots the temporal variations of $B_{\text{tot}} = |\mathbf{B}_{\text{tot}}|$, $B_{\text{trb}} = |\mathbf{B}_{\text{trb}}|$, and $B_{\text{reg}} = |\mathbf{B}_{\text{reg}}|$ averaged over the whole computational domain for all magnetized models. SN feedback creates the turbulent component from the regular component, while background shear tends to increase the regular component at the expense of the turbulent component. Note that the turbulent component saturates at $B_{\text{trb}} \sim 3 \mu\text{G}$, while the regular (and thus total) component grows secularly with time. The domain-averaged field strength is largely independent of the spiral-arm forcing. Figure 19(b) plots the temporal changes of the density-weighted magnetic fields in the arm region (with $\langle \Sigma \rangle$ larger than the mean value) and interarm region (with $\langle \Sigma \rangle$ smaller than the mean value) at $t = 150\text{--}700 \text{ Myr}$ for model F20B10. Overall, the magnetic fields in the arm are about 2.5 time stronger and thus grow more strongly than in the interarm regions.

Table 3 gives the mean values of the regular, turbulent, and total magnetic fields averaged over $t = 200\text{--}600 \text{ Myr}$. The spatial averages are taken over the whole domain for model F00B10 and over the arm and interarm regions, separately, for models F10B10 and F20B10. The regular component has $|B_{\text{reg},y}| > |B_{\text{reg},x}| \gg |B_{\text{reg},z}|$. Although the regular fields are dominated by the y -component, the turbulent fields are comparable in all directions. Note that $B_{\text{reg},x} < 0$ and $B_{\text{reg},y} > 0$ for all models, implying that the mean fields are trailing and inclined relative to the arm (or y -direction). The inclination angle of the regular magnetic fields relative to the arm is $\theta_B \equiv -\tan^{-1}(B_{\text{reg},x}/B_{\text{reg},y}) \sim 10^\circ$ in model F00B10, while $\theta_B \sim 7^\circ$ in the arm region and $\theta_B \sim 20^\circ$ in the interarm regions, insensitive to the arm strength, in models F10B10 and F20B10. The mean magnetic fields follow trailing gaseous spurs or filaments in the interarm region, while being roughly parallel to the arm in the arm region (see Figure 2).

Figure 20 plots the profiles in x (i.e. vs. offset from the arm) of the strength of the total, regular, and turbu-

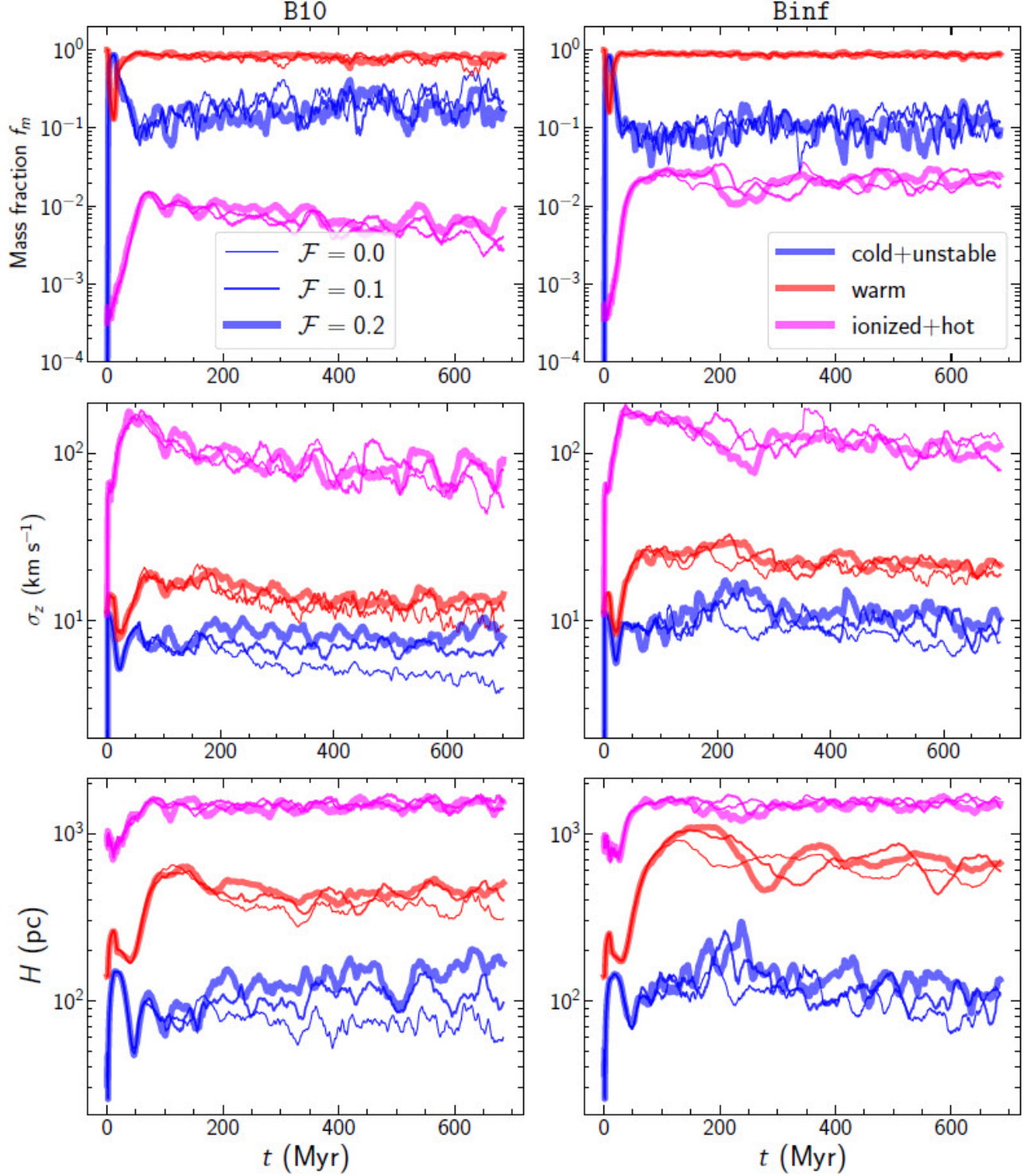


Figure 18. Comparison of temporal evolution of gas properties, divided by thermal phase: (top) the mass fractions f_m , (middle) the density-weighted vertical velocity dispersions σ_z , and (bottom) the density-weighted scale heights H , for (left) magnetized and (right) unmagnetized models. In each panel, we separate cold plus unstable ($T < 5050$ K; blue), warm ($5050 \text{ K} < T < 2 \times 10^4$ K; red), ionized plus hot phases ($T > 2 \times 10^4$ K; pink). Thick, intermediate, and thin lines correspond to the models with $\mathcal{F} = 0.2, 0.1$, and 0 , respectively.

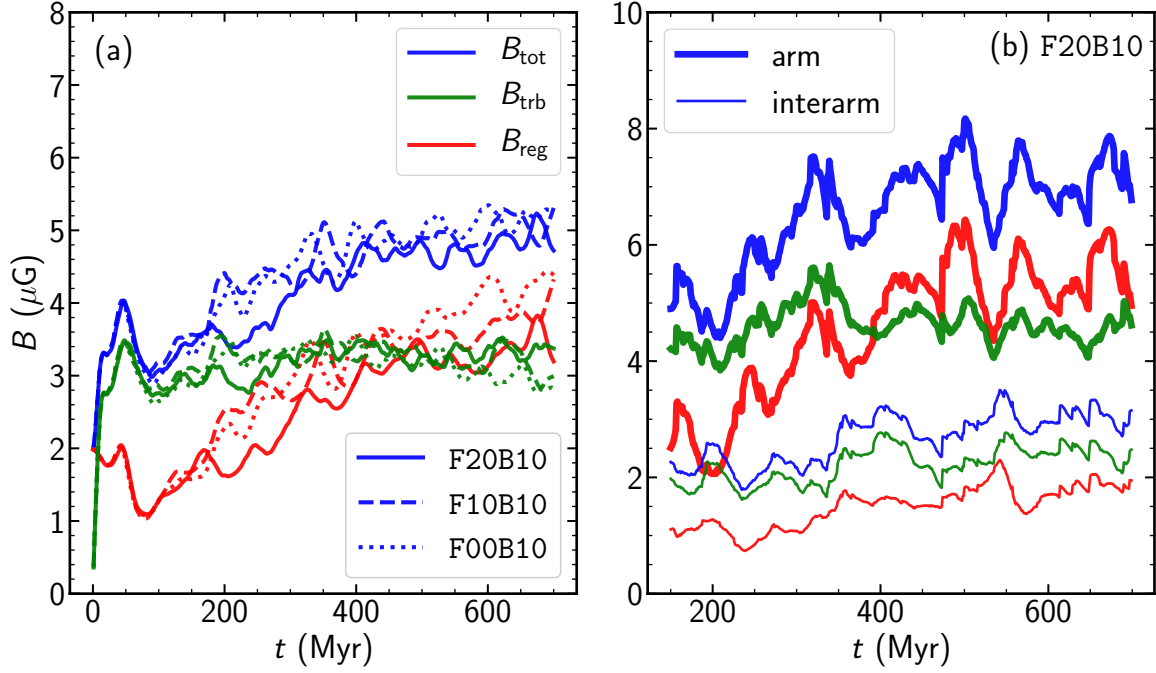


Figure 19. Temporal variations of the density-weighted, total (B_{tot}), turbulent (B_{trb}), and regular (B_{reg}) components of magnetic fields averaged over (a) the whole simulation domain for all magnetized models, and (b) the arm and interarm regions, separately, for model F20B10. While the turbulent fields saturate early, the regular and total components exhibit a secular growth. The magnetic fields are stronger in the arm, by about a factor of 2.5, than in the interarm region.

Table 3
Regular, Turbulent, and Total Magnetic Fields

Model (1)	Component (2)	B_{reg} (3)		B_{trb} (4)		B_{tot} (5)	
		Arm	Interarm	Arm	Interarm	Arm	Interarm
F00B10	total	3.29 ± 0.94		3.26 ± 0.43		4.70 ± 0.78	
	x-comp.	-0.58 ± 0.13		1.77 ± 0.27		1.89 ± 0.27	
	y-comp.	3.22 ± 0.95		2.33 ± 0.37		4.03 ± 0.81	
	z-comp.	0.00 ± 0.16		1.41 ± 0.23		1.43 ± 0.24	
F10B10	total	4.85 ± 1.80	2.01 ± 0.88	4.41 ± 0.62	2.53 ± 0.53	6.68 ± 1.56	2.53 ± 0.53
	x-comp.	-0.60 ± 0.15	-0.60 ± 0.14	2.41 ± 0.33	1.49 ± 0.26	2.49 ± 0.33	1.49 ± 0.26
	y-comp.	4.79 ± 1.82	1.89 ± 0.90	2.90 ± 0.51	1.74 ± 0.42	5.69 ± 1.60	1.74 ± 0.42
	z-comp.	0.00 ± 0.28	0.00 ± 0.13	2.24 ± 0.46	1.04 ± 0.30	2.25 ± 0.46	1.04 ± 0.30
F20B10	total	4.62 ± 2.17	1.63 ± 0.89	4.85 ± 1.06	2.27 ± 0.70	6.86 ± 2.09	2.27 ± 0.70
	x-comp.	-0.57 ± 0.17	-0.57 ± 0.12	2.74 ± 0.57	1.44 ± 0.38	2.81 ± 0.56	1.44 ± 0.38
	y-comp.	4.56 ± 2.21	1.49 ± 0.93	3.08 ± 0.73	1.47 ± 0.52	5.61 ± 2.07	1.47 ± 0.52
	z-comp.	0.03 ± 0.30	-0.02 ± 0.12	2.51 ± 0.65	0.92 ± 0.39	2.53 ± 0.66	0.92 ± 0.39

Note. — The mean values and standard deviations are taken over $t = 200\text{--}600$ Myr. Columns 3-5: density-weighted regular, turbulent, and total magnetic fields, respectively (μG). The arm and interarm regions are defined as the regions with $\langle \Sigma \rangle / \langle \Sigma \rangle_m$ larger and smaller than unity, respectively.

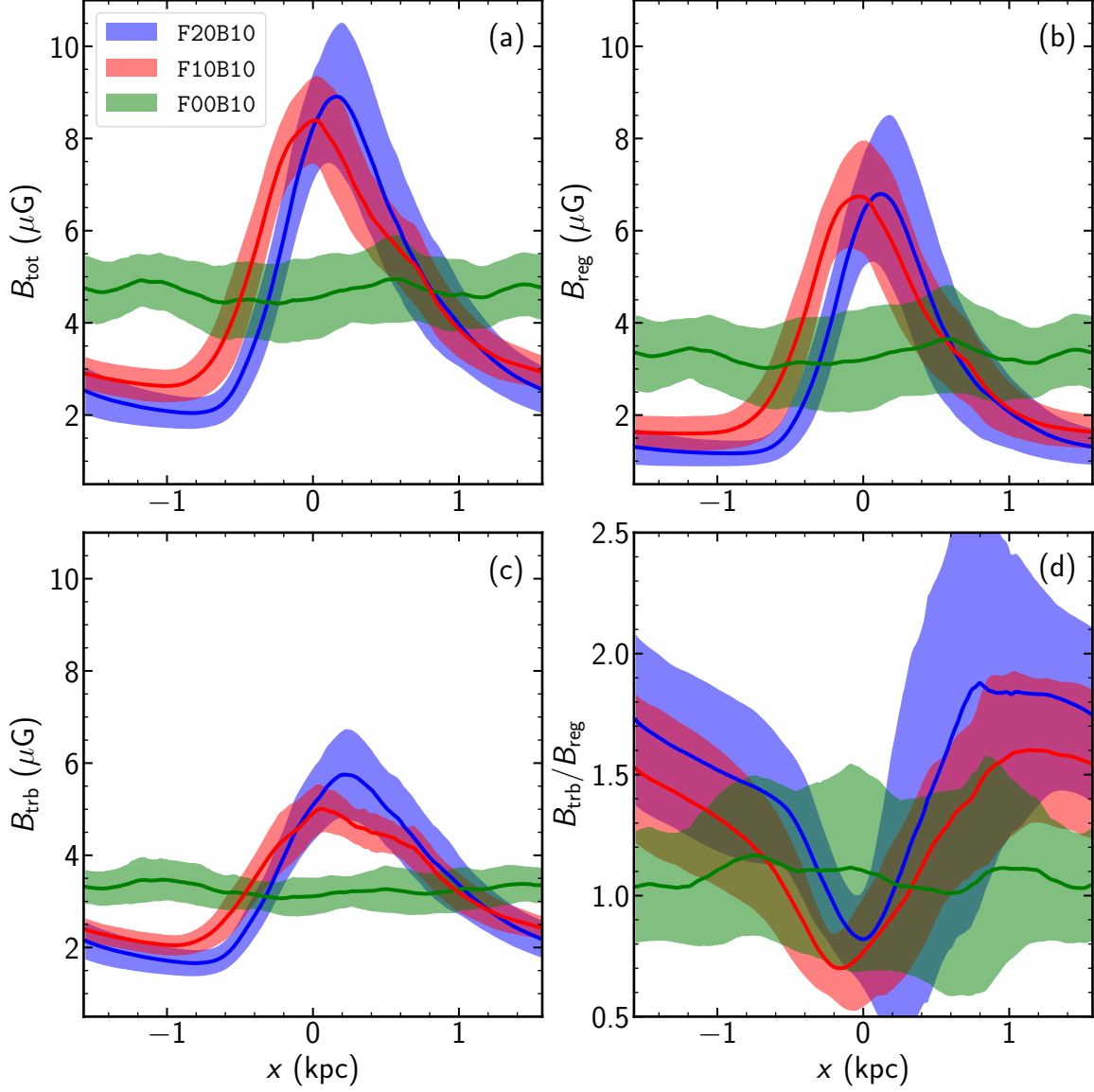


Figure 20. Profiles perpendicular to the arm of (a) total, (b) regular, (c) turbulent components of magnetic fields, and (d) the ratio of the turbulent to regular component in the magnetized models. The solid lines and colored shades give the mean and standard deviations over $t = 200\text{--}600$ Myr, respectively.

lent fields, as well as the ratio $B_{\text{trb}}/B_{\text{reg}}$ for all magnetized models. The solid lines give the mean values over $t = 200\text{--}600$ Myr, while the colored shades represent the standard deviations. In model F00B10, $B_{\text{tot}} \sim 4.7\mu\text{G}$ and $B_{\text{reg}} \sim B_{\text{trb}} \sim 3.3\mu\text{G}$, almost constant over x . The spiral-arm forcing compresses magnetic fields to $B_{\text{reg}} \sim 6.8\mu\text{G}$ at the arm density peak, insensitive to the arm strength, which is ~ 3 times stronger than the interarm regular fields. In the spiral-arm models, the turbulent component is stronger than the regular component almost everywhere, except near the upstream side of the arm region. This is because the turbulent magnetic fields are generated by the random gas motions driven by SN feedback that is most active in the feedback zone downstream from the arm. In model F20B10, $B_{\text{trb}}/B_{\text{reg}} \sim 1.4$ in the interarm region where the velocity dispersion is high due to low gas density.

Like the SFR, the strength of magnetic fields is correlated with the gas surface density. Figure 21 plots the

relationships between the gas surface density $\langle \Sigma \rangle$ and the (a) total, (b) regular, and (c) turbulent components of magnetic fields over $t = 200\text{--}600$ Myr for magnetized models. Clearly, magnetic fields are stronger in regions with higher gas density. The dashed lines are our best fits

$$B_{\text{tot}} = 4.63\mu\text{G} \left(\frac{\langle \Sigma \rangle}{10 \text{ M}_{\odot} \text{ pc}^{-1}} \right)^{0.58}, \quad (20a)$$

$$B_{\text{reg}} = 2.94\mu\text{G} \left(\frac{\langle \Sigma \rangle}{10 \text{ M}_{\odot} \text{ pc}^{-1}} \right)^{0.69}, \quad (20b)$$

$$B_{\text{trb}} = 3.35\mu\text{G} \left(\frac{\langle \Sigma \rangle}{10 \text{ M}_{\odot} \text{ pc}^{-1}} \right)^{0.49}, \quad (20c)$$

for the combined data of all magnetized models.

We note that even though B_{reg} is dominated by the y -component, the scaling of B_{reg} with $\langle \Sigma \rangle$ is sublinear, where a linear relation would apply for one-dimensional

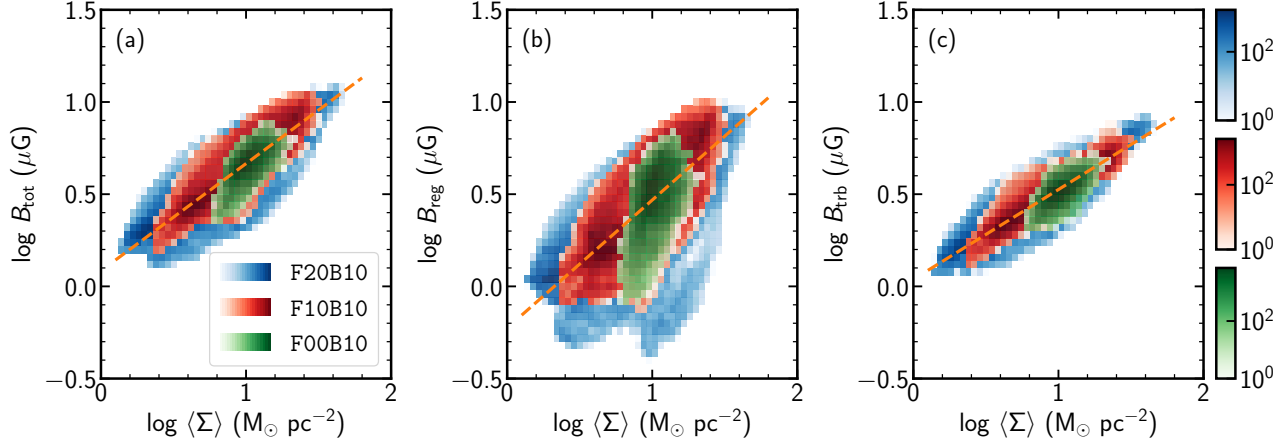


Figure 21. 2D histograms of the (a) total, (b) regular, and (c) turbulent components of magnetic fields and the gas surface density. Colorbars in blue, red, and green indicate the frequency of occurrence over $t = 200\text{--}600$ Myr for magnetized models with $\mathcal{F} = 0.2, 0.1$, and 0 , respectively. The dashed line in each panel draws the best fits, Equation (20), for the combined data.

compression in x of a uniform magnetic field B_y . This sublinear scaling is because magnetic fields can expand vertically when the gas is compressed horizontally, and indeed the enhancement of thermal and turbulent pressure from feedback in the arm aids in this vertical expansion.

4.5. Midplane Stress

When a disk is in a quasi-steady state, the force balance in the vertical direction requires that the weight of the gas under the total gravitational field should be supported by the total midplane stress. In the presence of magnetic fields, not only the magnetic pressure but also the vertical tension force $\partial(B_z^2/4\pi)/\partial z$ contribute to the magnetic forces, so that the relevant magnetic stress is $B^2/(8\pi) - B_z^2/(4\pi)$ (Boulares & Cox 1990; Piontek & Ostriker 2007; Ostriker et al. 2010). We measure the thermal, turbulent, and magnetic stresses at the midplane as

$$P_{\text{thm}} = \frac{1}{2\Delta z L_y} \iint_{z=-\Delta z}^{z=\Delta z} P dz dy, \quad (21a)$$

$$P_{\text{trb}} = \frac{1}{2\Delta z L_y} \iint_{z=-\Delta z}^{z=\Delta z} \rho v_z^2 dz dy, \quad (21b)$$

$$\Pi_{\text{mag}} = \frac{1}{2\Delta z L_y} \iint_{z=-\Delta z}^{z=\Delta z} \frac{B^2 - 2B_z^2}{8\pi} dz dy, \quad (21c)$$

respectively. Here, $\Delta z = 12.3$ pc refers to the grid spacing in the z -direction. In Π_{mag} , the tension term is about 17% of the magnetic pressure term in our simulations. The total midplane stress is $P_{\text{tot}} = P_{\text{thm}} + P_{\text{trb}} + \Pi_{\text{mag}}$.

We also measure the total weight of the gas as $\mathcal{W}_{\text{tot}} = \mathcal{W}_{\text{ext}} + \mathcal{W}_{\text{self}}$, where

$$\mathcal{W}_{\text{ext}} = \frac{1}{2} \iint_{z=-L_z/2}^{z=L_z/2} \rho \left| \frac{d\Phi_{\text{ext}}}{dz} \right| dz dy, \quad (22a)$$

$$\mathcal{W}_{\text{self}} = \frac{1}{2} \iint_{z=-L_z/2}^{z=L_z/2} \rho \left| \frac{d\Phi_{\text{self}}}{dz} \right| dz dy, \quad (22b)$$

representing the gas weight under the external gravity or self-gravity alone, respectively.

Figure 22 plots the relationship between P_{tot} and \mathcal{W}_{tot}

as well as the ratios $\mathcal{W}_{\text{ext}}/\mathcal{W}_{\text{tot}}$ and $\mathcal{W}_{\text{self}}/\mathcal{W}_{\text{tot}}$ as functions of x for the magnetized models over $t = 200\text{--}600$ Myr: the distributions are similar for the unmagnetized models. As expected, $P_{\text{tot}} \approx \mathcal{W}_{\text{tot}}$ within 12%, demonstrating that the disks are overall in dynamical equilibrium in the vertical direction. On average, $\mathcal{W}_{\text{self}} \approx 0.24\mathcal{W}_{\text{tot}}$ for the magnetized models and $\mathcal{W}_{\text{self}} \approx 0.20\mathcal{W}_{\text{tot}}$ for the unmagnetized models since the latter have higher Σ_{SFR} and thus lower gas mass. Inside the arm, $\mathcal{W}_{\text{self}}/\mathcal{W}_{\text{tot}}$ increases up to 0.30 and 0.27 in models F20B10 and F20Binf, respectively. This demonstrates that the gas weight in our models is dominated by the external gravity rather than self-gravity even inside the spiral arms.

Figure 23 plots the profiles in x of the mean values and standard deviations of (upper panels) the total midplane stress P_{tot} as well as (lower panels) the thermal, turbulent, and magnetic stresses, over $t = 200\text{--}600$ Myr. The left and right panels correspond to the magnetized and unmagnetized models, respectively. Columns 5–8 in Table 1 give the mean values and standard deviations of the various midplane stresses averaged spatially in the x -direction and temporally over $t = 200\text{--}600$ Myr.

The magnetized models have a higher total midplane stress, by a factor of ~ 1.3 on average, than the unmagnetized counterpart. This is because they contain more gas (Figure 17) with a larger scale height (Table 2), and thus have higher gas weight than the unmagnetized counterparts. In the magnetized models, the magnetic stress closely follows the $\langle \Sigma \rangle$ distribution shown in Figure 11(a) and has $\Pi_{\text{mag}} \sim (0.39 - 0.45)P_{\text{tot}}$ on average, while the thermal and turbulent pressures are larger in the region with stronger star formation (and SN feedback; see Figure 12). The thermal and turbulent pressures are individually higher in the unmagnetized models, by a factor of ~ 1.1 and 1.5 , respectively, than in the magnetized models, although the addition of the magnetic stress makes the total larger. All the stresses are almost flat in the x -direction in the no-arm models, and higher in the arm region owing to stronger self-gravity.

Figure 24 plots a 2D histogram of the total midplane stress P_{tot} and the gas surface density $\langle \Sigma \rangle$ for all models with spiral forcing. The colorbar represents the frequency of occurrence over $t = 200\text{--}600$ Myr. The dashed

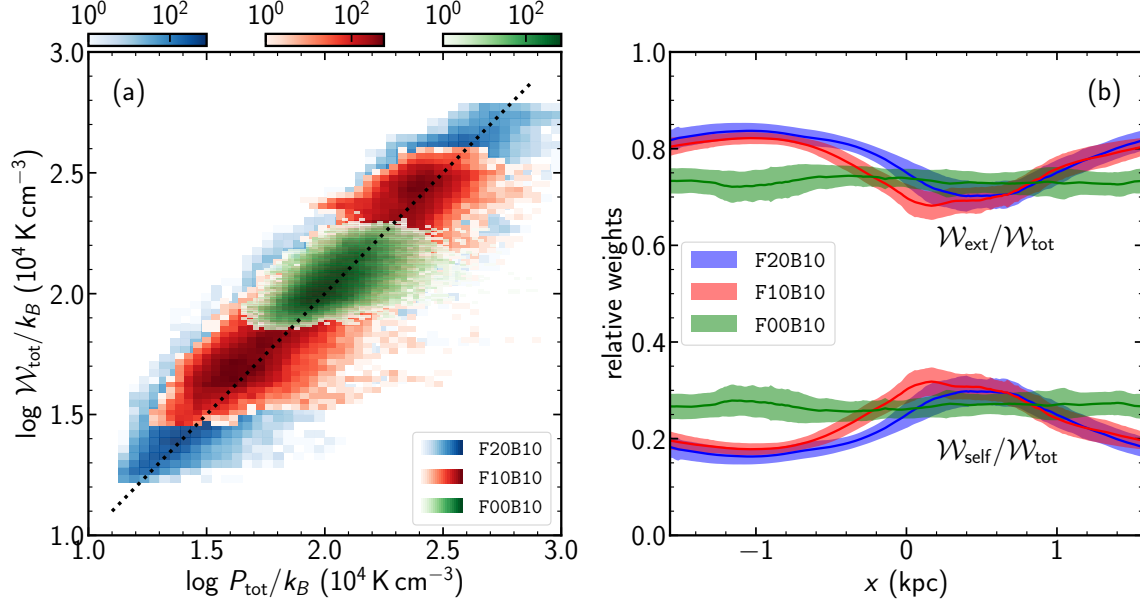


Figure 22. Gas weight and midplane pressure for all magnetized models. (a) 2D histograms of the total midplane stress P_{tot} and the total gas weight \mathcal{W}_{tot} , and (b) profiles of the relative contributions to the total gas weight from external gravity (\mathcal{W}_{ext}) and self-gravity ($\mathcal{W}_{\text{self}}$). The dashed line in (a) corresponds to $\mathcal{W}_{\text{tot}}/P_{\text{tot}} = 1$, and colorbars indicate the frequency of occurrence over $t = 200\text{--}600$ Myr. In (b), the solid lines and colored shades give the mean and standard deviations over $t = 200\text{--}600$ Myr, respectively.

line is the best fit

$$P_{\text{tot}} = 2.23 \times 10^4 k_B \text{ cm}^{-3} \text{ K} \left(\frac{\langle \Sigma \rangle}{10 \text{ M}_{\odot} \text{ pc}^{-2}} \right)^{1.11}. \quad (23)$$

In spite of the large variations of both surface density and pressure as the gas flows from interarm to arm and back (Figures 11 and 23), there is a nearly-linear relationship between P_{tot} and $\langle \Sigma \rangle$. The basic reason for this is that the vertical ISM weight \mathcal{W}_{tot} is dominated by $\mathcal{W}_{\text{ext}} \propto \langle \Sigma \rangle$, and since dynamical equilibrium is satisfied, the total stress (which must balance \mathcal{W}_{tot}) must vary as $P_{\text{tot}} \propto \langle \Sigma \rangle$. We note that the proportionality coefficient in Equation (23) is set by the vertical gravitational field of the background stars (see Equation (22)), which varies only tens of percent between arm and interarm. The coefficient would increase (decrease) in a galactic region where the vertical gravity from the stellar disk is higher (lower).

It is interesting to explore the relationship between the SFR surface density and the midplane stresses. For this purpose, we first calculate the average values $P_c(x_i) = w_{\text{bin}}^{-1} \int_{x_i - w_{\text{bin}}/2}^{x_i + w_{\text{bin}}/2} P_c dx$ in the 15 bins, as we did for the SFR surface density in Section 4.2. Here, the subscript “c” denotes “tot”, “thm”, “trb”, and “mag” for the respective midplane stress. We then measure the feedback “yields”

$$\eta_c \equiv \frac{P_c(x_i)}{\Sigma_{\text{SFR}}(x_i)}; \quad (24)$$

these yields η have velocity units, but can be converted to the scaled values adopted in Kim et al. (2013) and Kim & Ostriker (2015b) by multiplying by 4.8×10^{-3} . When the numerical data for models with $\mathcal{F} = 0.1$ and 0.2 are combined, and defining $\Sigma_{\text{SFR},-3} = \Sigma_{\text{SFR}}(x_i)/(10^{-3} \text{ M}_{\odot} \text{ pc}^{-2} \text{ Myr}^{-1})$, our magnetized models yield $\eta_{\text{tot}} = 1880 \text{ km s}^{-1} \Sigma_{\text{SFR},-3}^{-0.17}$, $\eta_{\text{thm}} = 693 \text{ km s}^{-1} \Sigma_{\text{SFR},-3}^{-0.43}$, $\eta_{\text{trb}} = 527 \text{ km s}^{-1} \Sigma_{\text{SFR},-3}^{-0.10}$, $\eta_{\text{mag}} =$

$187 \text{ km s}^{-1} \Sigma_{\text{SFR},-3}^{1.00}$, while the unmagnetized models give $\eta_{\text{tot}} = 1380 \text{ km s}^{-1} \Sigma_{\text{SFR},-3}^{-0.36}$, $\eta_{\text{thm}} = 558 \text{ km s}^{-1} \Sigma_{\text{SFR},-3}^{-0.36}$, $\eta_{\text{trb}} = 531 \text{ km s}^{-1} \Sigma_{\text{SFR},-3}^{-0.14}$. For a reference value of $\Sigma_{\text{SFR},-3} = 3.5$ (see Table 1), these correspond to $\eta_{\text{tot}} \approx 1519 \text{ km s}^{-1}$, $\eta_{\text{thm}} \approx 404 \text{ km s}^{-1}$, $\eta_{\text{trb}} \approx 464 \text{ km s}^{-1}$, and $\eta_{\text{mag}} \approx 654 \text{ km s}^{-1}$ for the magnetized models, showing that the magnetic yield is about 45% of the total.

Figure 25 plots the 2D histogram of $\Sigma_{\text{SFR}}(x_i)$ and $P_{\text{tot}}(x_i)$ for all models with spiral forcing. The colorbar represents the frequency of occurrence over $t = 200\text{--}600$ Myr. Notwithstanding the large scatter caused by the y -averaging, $P_{\text{tot}}(x_i)$ has a good correlation with $\Sigma_{\text{SFR}}(x_i)$. The dashed line draws our best fit,

$$\Sigma_{\text{SFR}} = 1.64 \times 10^{-3} \text{ M}_{\odot} \text{ pc}^{-2} \text{ Myr}^{-1} \left(\frac{P_{\text{tot}}/k_B}{10^4 \text{ cm}^{-3} \text{ K}} \right)^{1.24}. \quad (25)$$

This is very close to Equation (26) from Kim et al. (2013), plotted as a solid line, which was obtained from unmagnetized models with no spiral forcing, and a two-phase ISM model. This suggests that star formation in our spiral-arm simulations is self-regulated, similarly to Kim et al. (2013), in such a way that it keeps the disk in thermal, turbulent, and dynamical equilibrium (see also Ostriker et al. 2010; Kim et al. 2011). With P_{tot} nearly linearly dependent on $\langle \Sigma \rangle$ from Equation (23), Equation (25) is consistent with the relationship between Σ_{SFR} and Σ indicated by Equation (16).

5. SUMMARY AND DISCUSSION

5.1. Summary

Spiral arms greatly affect gas flows, magnetic fields, and star formation in disk galaxies. Two unsolved problems for spiral galaxies are (1) whether the spiral arms enhance the SFR in the disks or not and (2) how gaseous spurs/feathers perpendicular to arms form and evolve. To address these issues, in this paper we have extended

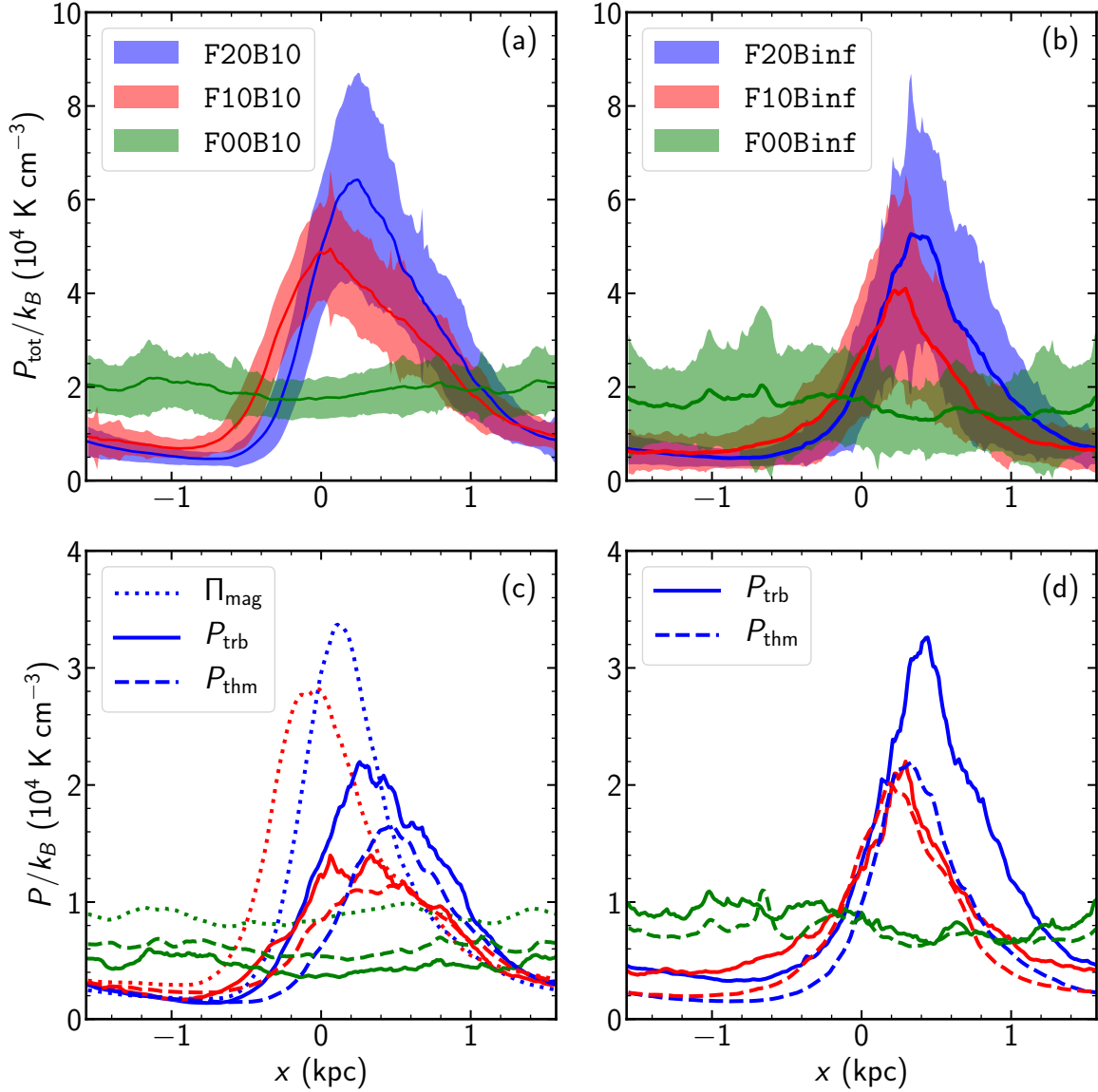


Figure 23. Profiles perpendicular to the arm of (a,b) the total midplane stress and (c,d) various midplane stresses for the (left) magnetized and (right) unmagnetized models. Blue, red, and green correspond to models with $\mathcal{F} = 0.2, 0.2, \text{ and } 0$, respectively. The lines and colored shades represent the mean values and standard deviations over $t = 200\text{--}600$ Myr. For clarity, only mean values are shown in (c) and (d).

the TIGRESS simulations of Kim & Ostriker (2017) to include the effect of a stellar spiral-arm potential. TIGRESS is a numerical framework that accurately handles the formation and evolution of star clusters (represented as star particles in the simulation) and the heating plus SN explosions they create. The TIGRESS framework allows us to model the turbulent, magnetized, multiphase (cold-warm-hot), differentially-rotating, self-gravitating, vertically-stratified ISM self-consistently with star formation and key feedback effects produced by massive stars. We adopt the local spiral-arm coordinates of Roberts (1969) where the two orthogonal axes in the galactic plane correspond to the directions perpendicular ($\hat{\mathbf{x}}$) and parallel ($\hat{\mathbf{y}}$) to a local segment of a spiral arm, respectively, while the third coordinate ($\hat{\mathbf{z}}$) is perpendicular to the galactic plane. We derive the equations of motions for star particles in the spiral-arm coordinates (Appendix A), and use them in the simulations.

Our simulation domain is a rectangular box corotat-

ing with the arm. The box size L_x in the x -direction is set equal to the arm-to-arm distance. We represent the spiral arm using a fixed gravitational potential of a simple sinusoidal shape (Equation (9)), with its minimum occurring at the middle of the box ($x = 0$). All models have initial gas surface density $\Sigma_0 = 13 \text{ M}_\odot \text{ pc}^{-2}$, similar to that in the Solar neighborhood and other “mid-disk” galactic environments. For magnetized models, the disks are initially threaded by magnetic fields parallel to the spiral arm. We consider 6 models that differ in the arm strength and magnetic field strength which are characterized by the dimensionless parameters \mathcal{F} and β , respectively (Equations (12) and (13)). In order to avoid transients caused by a sudden introduction of the arm potential, we increase its amplitude slowly to the full strength achieved at $t = 200$ Myr. All models are run up to $t = 700$ Myr, long enough for the disk to reach a quasi-steady state.

The main results can be summarized as follows.

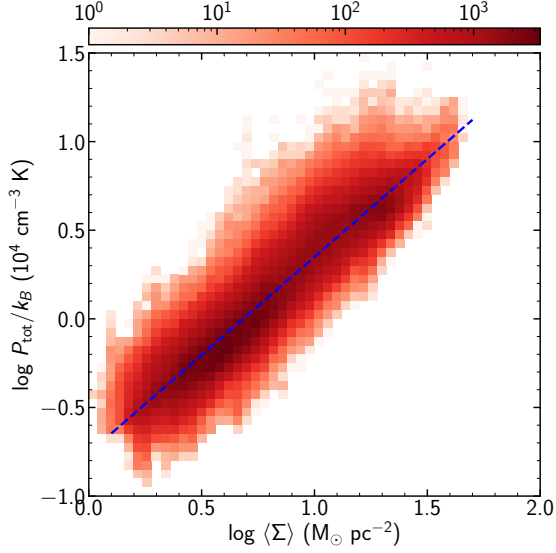


Figure 24. 2D histogram of the total midplane stress P_{tot} and the gas surface density $\langle \Sigma \rangle$ averaged along the y -direction for all models with spiral forcing ($\mathcal{F} \neq 0$). The colorbar indicates the frequency of occurrence over $t = 200\text{--}600$ Myr. The dashed line draws the best fit, Equation (23).

1. *Overall Evolution* – As the amplitude of the spiral potential grows with time, a dense ridge forms in the region slightly downstream from the potential minimum. Gathering of individual filaments of sheared gas and shells created by expanding superbubbles contributes to the formation of this ridge. Compared to the interarm region, the gas in the arm is denser and colder, has stronger magnetic fields and midplane pressure, and is the locus of most star formation in the simulation domain. Star particles formed in the arm exhibit a spatial gradient with respect to age amounting to $dx_m/dt_m \sim 9 \pm 4 \text{ pc Myr}^{-1}$ on average, with x_m and t_m denoting the mass-weighted mean position and age of star particles, respectively. Arm star formation is usually clustered, with SNe injecting thermal and kinetic energy in the downstream feedback zones to create superbubbles. These interact and are advected by the background flow to produce turbulence throughout the simulation domain, with the larger superbubbles breaking out of the disk to vent hot gas through chimneys. The system rapidly reaches a quasi-steady state in which turbulence driven by SN feedback balances dissipation, and the heating (radiation plus SN energy input) balances cooling. Without gas inflows from outside the domain, continued star formation and mass loss through the vertical boundaries make the gas mass and SFR decrease with time in our simulations.
2. *Spurs/Feathers* – Clustered and correlated star formation in the arm produces expanding superbubbles that are distorted as they move downstream, with their boundaries turning to dense filaments attached to the spiral arm. While weak filaments are readily destroyed by nearby feedback, strong filaments survive and undergo collisions with neighboring ones, forming even denser, large-

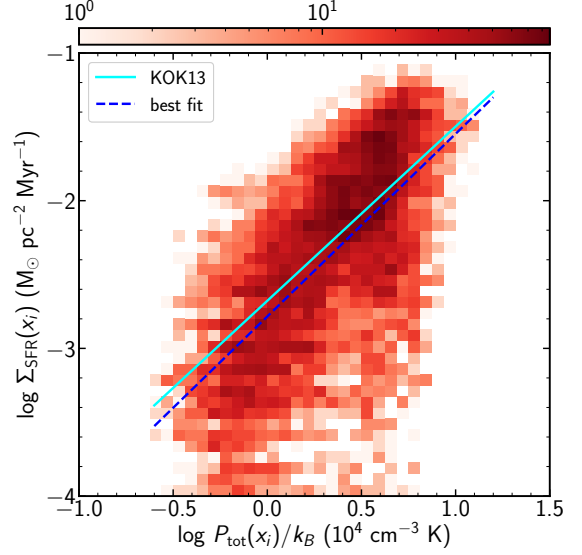


Figure 25. 2D histogram of the local SFR surface density $\Sigma_{\text{SFR}}(x_i)$ and the local midplane stress $P_{\text{tot}}(x_i)$ for all models with spiral-arm forcing ($\mathcal{F} \neq 0$). The colorbar indicates the frequency of occurrence over $t = 200\text{--}600$ Myr. The solid line draws Equation (26) of Kim et al. (2013), while the dashed line is our best fit, Equation (25).

scale structures. These dense structures, bounded on both sides by regions where feedback has cleared out gas (see Figures 1 and 9), resemble gaseous spurs/feathers seen in real disk galaxies with strong spirals. These feedback-induced spurs form regardless of the presence of magnetic fields. Spurs in our models protrude nearly perpendicularly from the arm and turn to a trailing configuration in the interarm region. In magnetized models, the magnetic field is generally parallel to the “long axis” of the spur. They are transient and last for ~ 30 Myr before being destroyed by nearby feedback and turbulence. Their mean spacing along the arm is $\sim 2\text{--}3$ kpc, tending to be larger in unmagnetized models with a weaker spiral-arm forcing.

3. *Star Formation* – In our models, more than 90% of star formation is concentrated in the arm, defined as the region where the gas surface density is above the mean value. The vertical distribution of star-forming positions are well described by an exponential function, with a scale height proportional to the SFR. The local SFR surface density Σ_{SFR} averaged along the y -direction is proportional roughly linearly to the local gas surface density Σ averaged along the y -direction (Equation (16)) and to the total midplane stress P_{tot} (Equation (25)), where the latter is also equal to the ISM vertical weight \mathcal{W}_{tot} . Compared to the no-arm counterpart, the global SFR surface density averaged over the entire domain is only modestly enhanced by the spiral-arm forcing, by respective factors of 1.6 and 1.2 in models F20B10 and F20Binf (which have $\mathcal{F} = 0.2$). This suggests that spiral arms do not trigger star formation much, but rather concentrate star-forming regions into narrow ridges. The local Σ_{SFR} in the arm is about an order of magnitude or more higher than in the interarm region. The weak dependence of Σ_{SFR} on \mathcal{F} is consistent with

the quasi-linear dependence of local Σ_{SFR} on the local Σ . The near-linear relationship we find between Σ_{SFR} and P_{tot} is quantitatively in agreement with results from our previous simulations (Figure 25).

4. *Magnetic Fields and Midplane Stress* – Turbulence driven by SN feedback stretches and twists magnetic fields to generate an irregular, turbulent component. Due to background shear, the regular magnetic fields are trailing, with a mean inclination angle of $\sim 7^\circ$ in the arm and $\sim 20^\circ$ in the interarm regions, relative to the spiral arm. Both regular and turbulent components of the magnetic field are strong inside the arm and weak in the interarm region, with their strength sublinearly proportional to the gas surface density (Equation (20)). In models with spiral-arm forcing, the turbulent magnetic component is stronger than the regular components especially in the interarm region, up to a factor of 1.5. Our disks are overall in local dynamical equilibrium in which the total midplane stress P_{tot} (with thermal, turbulent, and magnetic contributions) balances the gas weight \mathcal{W}_{tot} along the vertical direction (Figure 22). The contribution of self-gravity to the total gas weight $\mathcal{W}_{\text{self}}/\mathcal{W}_{\text{tot}}$ is 20–24% on average and 27–30% in the spiral-arm density peaks. Because the gas weight is dominated by $\mathcal{W}_{\text{ext}} \propto \Sigma$, the midplane stress P_{tot} is approximately linearly proportional to $\langle \Sigma \rangle$ (Equation (23)). The magnetic tension term in the vertical force balance is about $\sim 17\%$ of the magnetic pressure term in the midplane, while the magnetic stress amounts to about $\sim 40\%$ of P_{tot} .

5.2. Discussion

In our models, spiral-arm spurs form due to SN feedback in the interarm regions immediately downstream from arms, as a result of clustered and correlated arm star formation. This mechanism is different from the MJI of quasi-steady spiral arms proposed for spur formation by Kim & Ostriker (2002, 2006). In the MJI, spurs are nonlinear waves that grow via self-gravity. They collect material along the direction parallel to the arm, which is also parallel to the mean magnetic field. Thus, MJI-induced spurs are predicted to have magnetic fields perpendicular to their “long axis” and to be associated with converging velocity fields with amplitudes of order $\sim 10 \text{ km s}^{-1}$ (e.g., Kim & Ostriker 2002). This is in stark contrast to feedback-induced spurs, which would have magnetic fields parallel to the length of the spur, and could have larger converging velocities up to $\sim 50\text{--}100 \text{ km s}^{-1}$. In addition, spurs resulting from the MJI endure for a long time ($\sim 2\pi/\Omega_0 = 200 \text{ Myr}$) until they undergo gravitational fragmentation into bound clumps, while feedback-induced spurs are transient, being readily destroyed by subsequent feedback events. Nonlinear perturbations provided by feedback wipe out linear modes of MJI that might otherwise have grown in our simulations. Observations of small-scale magnetic and velocity fields around spurs/feathers may provide tell-tale signs regarding whether they are produced by MJI or SN feedback.

In our simulations, we find no evidence for the growth of WI in arms downstream from spiral shocks, a mechanism that was proposed for inducing spur/feather for-

mation by Wada & Koda (2004). As shown by Kim et al. (2014), the WI develops as PV generated from deformed spiral shocks accumulates successively as orbiting gas passes through shocks periodically. This requires that the arm and shock fronts have a steady pattern speed and that the PV remains coherent before and after the shock fronts. In the present simulations, however, shock fronts oscillate around the mean position in the x -direction, making the density profile broader than the isothermal counterpart (see Figure 11). More importantly, strong turbulence driven by SN feedback rapidly mixes neighboring vortices with different polarity produced at a deformed shock front. This mixing is hostile to the growth of WI. The presence of magnetic fields and vertical shear also help to suppress the WI in our models (see also, Kim & Ostriker 2006; Kim et al. 2015; Sormani et al. 2017).

The number of spurs in our magnetized models is typically 2 or 3, corresponding to a mean spacing of $\lambda \sim 2\text{--}3 \text{ kpc}$. There are many factors including arm pitch angle and strength, angular velocity, and gas surface density that may affect the spur spacing significantly. In particular, the spacing of feedback-induced spurs should be affected by characteristic gravitational scales, such that the spacing of correlated star formation varies inversely with Σ or Σ_{SFR} . This is supported by recent observational results. By analyzing CO data for M51, for instance, Schinnerer et al. (2017) identified nine molecular spurs with $\lambda \sim 0.33 \text{ kpc}$ in the northern spiral arm located $\sim 2.3 \text{ kpc}$ away from the galaxy center. This small value of λ in M51 is likely due to high gas surface density $\Sigma \sim 160 \text{ M}_\odot \text{ pc}^{-2}$ and high SFR surface density $\Sigma_{\text{SFR}} \sim 0.15 \text{ M}_\odot \text{ pc}^{-2} \text{ Myr}^{-1}$ (Leroy et al. 2017), which are about an order of magnitude larger than the values in model F20B10. On the other hand, Figure 1 of Kreckel et al. (2018) shows that the spiral arms in M74 have prominent molecular spurs with $\lambda \sim 1\text{--}2 \text{ kpc}$ in the regions at $R \sim 5\text{--}6 \text{ kpc}$ from the galaxy center, where both Σ and Σ_{SFR} are somewhat smaller than in the arms of M51.

That the total SFR in our simulations is insensitive to the arm strength is consistent with the observational results that the SFR is not much different in flocculent and grand-design spiral galaxies (Elmegreen & Elmegreen 1986) and that arm and interarm regions have similar gas depletion time (Foyle et al. 2010; Eden et al. 2013). This is also entirely consistent with the recent work of Tress et al. (2020), who ran three-dimensional simulations of an interacting galaxy similar to the M51 system, and found that tidal interactions redistribute gas across the disk, and concentrate star formation within the tidally-induced arms. However, the total SFR is affected by less than a factor two (see their Figure 15), as we have also found. Theoretically, the insensitivity of the total SFR to the arm strength is related to the fact that the SFR surface density is quasi-linearly proportional to the gas surface density. The quasi-linear relationship between Σ_{SFR} and Σ indicates a roughly constant gas depletion time, consistent with recent resolved observations of external galaxies (e.g., Leroy et al. 2017; Kreckel et al. 2018; see also Wong & Blitz 2002; Bigiel et al. 2008; Schrubba et al. 2011, but note that star formation is as strongly correlated with stellar content as gas content – e.g. Leroy et al. 2008; Bolatto et al. 2017). This in

turn implies that the arm star formation in our models corresponds to the regime where the external gravity from stars is more important than gaseous self-gravity in establishing the vertical force balance (Ostriker et al. 2010; Kim et al. 2011, 2013). In gas-rich galaxies at high redshift or starbursts in the local Universe, there may be regions where self-gravity dominates the weight, such that the equilibrium model for regulation of star formation yields $\Sigma_{\text{SFR}} \propto \Sigma^2$ (Ostriker & Shetty 2011; Shetty & Ostriker 2012). Any physical process (including a spiral forcing, tidal interactions, or mergers) that concentrates gas enough to become self-gravitating is expected to enhance the total SFR significantly.

The fairly well-defined age gradient of young star clusters seen in our simulations may be a consequence of adopting a fixed gravitational potential for spiral arms. The presence of the age gradient appears to depend on the nature of the spiral potential. Using numerical simulations, Dobbs & Pringle (2010) showed that galaxies with quasi-stationary spiral density waves exhibit a clear monotonic age gradient, while those with tidally-induced, transient arms do not. They proposed that the presence or absence of the age gradient can be used as a potential discriminant for the nature of spiral arms. Shabani et al. (2018) found that NGC 1566, a grand-design barred-spiral galaxy with bisymmetric arms, has a noticeable age gradient across the spiral arms, suggesting that the arms may represent quasi-stationary density waves with a constant pattern speed, as envisaged by Lin & Shu (1964, 1966). For M51, on the other hand, they found star clusters with different ages are peaked almost at the same locations, although older clusters spread more widely (see also Kaleida & Scowen 2010; Chandar et al. 2017). The lack of age gradient for the young star clusters in M51 is presumably because its tidally-driven arms have not yet reached a steady state, and are still changing their amplitudes and pattern speed (Shabani et al. 2018).

Radio synchrotron observations of external disk galaxies reveal that the pitch angles of large-scale magnetic fields are correlated with those of the gaseous arms, with the former systematically larger by $\sim 5^\circ\text{--}10^\circ$, on average, than the latter (Van Eck et al. 2015; Frick et al. 2016; see also the review by Beck 2016). This is consistent with our numerical results that magnetic fields in the arm are inclined relative to the gaseous arm. In our models, the inclination angle θ_B of magnetic fields is determined by the competition among three agents: spiral arm compression, SN feedback, and background shear. Spiral compression and shear tend to decrease θ_B , while SN feedback increases θ_B by creating quasi-radial fields from quasi-azimuthal magnetic fields. SN feedback and shear yield quasi-equilibrium regular fields with $\theta_B \sim 13^\circ$ in models without a spiral forcing, and the spiral compression (decompression) decreases (increases) θ_B to $\sim 7^\circ$ ($\sim 20^\circ$) in the arm (interarm) regions.

Our simulations show that the strength of magnetic fields are correlated with the gas surface density and SFR surface density via Equations (16) and (20). Under the assumption of equipartition between the energy densities of magnetic fields and cosmic rays, Tabatabaei et al. (2013) used synchrotron emission to estimate the field strength across the disk of NGC 6946, finding that

$B_{\text{tot}} \propto \Sigma_{\text{SFR}}^{0.14}$ and $B_{\text{tot}} \propto \Sigma^{0.23}$. These are shallower than our numerical results $B_{\text{tot}} \propto \Sigma_{\text{SFR}}^{0.54}$ and $B_{\text{tot}} \propto \Sigma^{0.61}$ (see Equation (20)). The shallow relations reported in observations suggest that the arm-to-interarm contrast of magnetic fields is very low (~ 1.3 in M51; see Fletcher et al. 2011). However, we caution that this shallow relation might be a consequence of the assumption of the energy equipartition. There is no fundamental physical reason for equipartition to hold, especially at small scale (e.g. Stepanov et al. 2014). If instead cosmic rays are in fact more uniform than magnetic fields, then the true B - Σ relationship should be steeper; if magnetic fields and cosmic rays are anticorrelated, then the relation would be much steeper.

Finally, we remark on a few important caveats of our simulations. First, our current models adopt local, spiral-arm coordinates which assume quite tightly-wound arms and neglect curvature terms. The local models also cannot capture self-gravitating modes with wavelength longer than the x -width of the simulation box. Although we do not expect that qualitative results would change, to capture missing effects it is desirable to run global simulations with radially-varying surface density, adopting more realistic arm pitch angles ($\sim 20^\circ\text{--}30^\circ$). Second, by taking the diode-like vertical boundary conditions, our models do not allow for gas accretion from outside the simulation box and thus result in a secular decrease of the SFR over time. Observations indicate that the gas accretion rate to the Milky Way is $\sim 0.1\text{--}0.4 \text{ M}_\odot \text{ yr}^{-1}$ for the cold gas (Putman et al. 2012) and $\sim 1 \text{ M}_\odot \text{ yr}^{-1}$ including the ionized gas (Lehner & Howk 2011). Inclusion of accreted gas can offset the long-term decline of the gas mass via star formation and outflows in our simulations. Third, in the current TIGRESS framework that we adopt, SN explosions are the only form of feedback that directly contributes to the turbulent pressure. In reality, other forms of feedback such as stellar winds and ionizing radiation help to pressurize the ISM in star-forming regions before the onset of first SNe. Although the total (lifetime) momentum injection from these sources is small compared to that from SNe, the immediate onset may help to limit collapse of dense gas. Inclusion of additional “early” feedback represents an important direction for future high-resolution simulations of star formation and the ISM in spiral galaxies.

We appreciate a thoughtful report from the referee. W.-T.K. gratefully acknowledges the assistance and hospitality provided by the Department of Astrophysical Sciences at Princeton University during his sabbatical visit when this paper was prepared. The work of W.-T.K. was supported by the National Research Foundation of Korea (NRF) grant funded by the Korea government (MSIT) (2019R1A2C1004857), with partial sabbatical support from the Simons Foundation under grant 510940 to E.C.O.. The work of C.-G.K. and E.C.O. was partially supported by grant NNX17AG26G from NASA. C.-G.K. also acknowledges support from the Simons Foundation Award No. 528307 (E.C.O.). Computational resources for this project were provided by Princeton Research Computing, a consortium including PICSciE and OIT at Princeton University.

Software: *Athena* (Stone et al. 2008), *numpy* (van der

Walt et al. 2011), `matplotlib` (Hunter 2007), `IPython` (Pérez & Granger 2007), `pandas` (McKinney 2010).

APPENDIX

EQUATIONS OF MOTION FOR STAR PARTICLES

Here we derive the equations of motion for sink/star particles in spiral-arm coordinates. We start from Newton's force equation in the inertial frame of reference

$$\ddot{\mathbf{R}} = -\nabla\Phi_{\text{tot}}, \quad (\text{A1})$$

where $\mathbf{R} = R\hat{\mathbf{R}} + z\hat{\mathbf{z}}$ is the coordinate vector in cylindrical coordinates and $\Phi_{\text{tot}} = \Phi_{\text{self}} + \Phi_{\text{ext}}$ is the total gravitational potential. We assume that the axisymmetric part Φ_0 of the total gravitational potential is separable from the remaining non-axisymmetric part Φ_1 such that $\Phi_{\text{tot}} = \Phi_0(R) + \Phi_1(R, \phi, z)$: the axisymmetric part Φ_0 is responsible for the galaxy rotation with angular frequency $\Omega = (R^{-1}d\Phi_0/dR)^{1/2}$, and Φ_1 can be regarded as perturbations to Φ_0 . Equation (A1) can then be rewritten as

$$(\ddot{R} - R\dot{\phi}^2 + R\Omega^2)\hat{\mathbf{R}} + (2\dot{R}\dot{\phi} + R\ddot{\phi})\hat{\phi} + \ddot{z}\hat{\mathbf{z}} = -\nabla\Phi_1. \quad (\text{A2})$$

Equation (A2) states that the specific angular momentum $L_z = R^2\dot{\phi}$ is constant if Φ_1 is axisymmetric.

In the Frame Rotating at Ω_p

We now consider a frame rotating at angular frequency $\Omega_p = \Omega_p\hat{\mathbf{z}}$ which is not necessarily same as the local angular frequency $\Omega_0 = \Omega(R_0)$. With a new angle variable $\phi_p \equiv \phi - \Omega_p t$, Equation (A2) becomes

$$(\ddot{R} - R\dot{\phi}_p^2)\hat{\mathbf{R}} + (2\dot{R}\dot{\phi}_p + R\ddot{\phi}_p)\hat{\phi} + \ddot{z}\hat{\mathbf{z}} = -\nabla\Phi_1 + R(\Omega_p^2 - \Omega^2)\hat{\mathbf{R}} - 2\Omega_p \times \dot{\mathbf{R}}, \quad (\text{A3})$$

where $\dot{\mathbf{R}}_p \equiv (\dot{R}, R\dot{\phi}_p, 0)$.

We set up a local Cartesian frame $(X, Y, Z) = (R - R_0, R_0\phi_p, z)$ centered at $(R_0, \Omega_p t, z)$, and make a local approximation such that $|X|, |Y - \dot{Y}_0 t|, |Z| \ll R_0$ and $|\dot{X}|, |\dot{Y} - \dot{Y}_0|, |\dot{Z}| \ll R_0\Omega_0$, where $\dot{Y}_0 \equiv R_0(\Omega_0 - \Omega_p)$ is the background rotational velocity seen in the rotating frame. Then, Equation (A3) is decomposed as

$$\ddot{X} = -\frac{\partial\Phi_1}{\partial X} + 2\Omega_0(\dot{Y} - \dot{Y}_0) + 2q\Omega_0^2 X, \quad (\text{A4a})$$

$$\ddot{Y} = -\frac{\partial\Phi_1}{\partial Y} - 2\Omega_0\dot{X}, \quad (\text{A4b})$$

$$\ddot{Z} = -\frac{\partial\Phi_1}{\partial Z}, \quad (\text{A4c})$$

where $q = -d\ln\Omega/d\ln R|_{R_0}$ is the shear parameter. When $\Omega_p = \Omega_0$, that is, in the frame rotating at the local angular frequency Ω_0 , Equation (A4) becomes Hill's equations, which can be integrated to yield

$$\frac{1}{2}(\dot{X}^2 + \dot{Y}^2 + \dot{Z}^2) - q\Omega_0^2 X^2 + \Phi_1 = \text{constant}, \quad (\text{A5})$$

corresponding to conservation of the total energy including the tidal potential $(-q\Omega_0^2 X^2)$.

Equation (A4) possesses solutions for epicycle orbits in the X - Y plane. In the absence of the external forcing ($\Phi_1 = 0$), Equations (A4a) and (A4b) can be integrated to yield the orbit in the $z = 0$ plane as

$$X = A\kappa_0 \sin(\kappa_0 t + B) + X_0, \quad (\text{A6a})$$

$$Y = 2A\Omega_0 \cos(\kappa_0 t + B) - q\Omega_0 X_0 t + \dot{Y}_0 t + Y_0, \quad (\text{A6b})$$

where A , B , X_0 , and Y_0 are constants to be determined subject to the initial conditions and $\kappa_0 = (4 - 2q)^{1/2}\Omega_0$ is the epicycle frequency. Note that the center of the epicycle (X_0, Y_0) drifts at a constant speed $-q\Omega_0 X_0 + \dot{Y}_0$ along the Y -direction due to the background rotation (\dot{Y}_0) and shear ($-q\Omega_0 X_0$).

In the Spiral-arm Coordinates

We now tilt the local (X, Y, Z) frame by an angle i to construct another rectangular frame (x, y, z) , where x and y refer to the directions perpendicular and parallel to a local arm segment, respectively, while z denotes the vertical direction. This is achieved by the coordinate transformation

$$\begin{pmatrix} X \\ Y \\ Z \end{pmatrix} = \begin{pmatrix} \cos i & -\sin i & 0 \\ \sin i & \cos i & 0 \\ 0 & 0 & 1 \end{pmatrix} \begin{pmatrix} x \\ y \\ z \end{pmatrix}. \quad (\text{A7})$$

Assuming that the arm is tightly wound with $\sin i \ll 1$, it is straightforward to transform Equation (A4) into the spiral-arm coordinates. Due to the constant drift of epicycle orbits, however, one should be careful in handling the

$-2q\Omega_0^2 y \sin i$ term originating from the last term of Equation (A4a). Even if $\sin i$ is small under the tightly wound approximation,

$$y \sin i \approx Y \sin i \approx (\dot{Y}_0 \sin i) t \quad (\text{A8})$$

can be of order unity for sufficiently large t , representing the drift of a guiding center due to galaxy rotation (Equation (A6b)). Keeping all the terms of order unity, Equation (A4) is transformed to

$$\ddot{x} = -\frac{\partial \Phi_1}{\partial x} + 2\Omega_0(\dot{y} - \dot{y}_0) + 2q\Omega_0^2(x - \dot{x}_0 t), \quad (\text{A9a})$$

$$\ddot{y} = -\frac{\partial \Phi_1}{\partial y} - 2\Omega_0(\dot{x} - \dot{x}_0), \quad (\text{A9b})$$

$$\ddot{z} = -\frac{\partial \Phi_1}{\partial z}, \quad (\text{A9c})$$

where $\dot{x}_0 = \dot{Y}_0 \sin i$ and $\dot{y}_0 = \dot{Y}_0$. These are the desired set of equations for star particles in the spiral-arm coordinates. The time t in the last term of Equation (A9a) can be identified as the age of each star particle. The corresponding equation for energy conservation reads

$$\frac{1}{2} |\dot{\mathbf{x}} - \dot{\mathbf{x}}_0|^2 - q\Omega_0^2(x - \dot{x}_0 t)^2 + \Phi_1 = \text{constant}, \quad (\text{A10})$$

with $\dot{z}_0 = 0$.

When $\Phi_1 = 0$, the x and y coordinates are separable from the z coordinate, and Equation (A9) can be integrated to give the epicycle orbit

$$x = a\kappa_0 \sin(\kappa_0 t + b) + \dot{x}_0 t + x_0, \quad (\text{A11a})$$

$$y = 2a\Omega_0 \cos(\kappa_0 t + b) + (\dot{y}_0 - q\Omega_0 x_0)t + y_0, \quad (\text{A11b})$$

where a , b , x_0 , and y_0 are integration constants determined by the initial conditions. It is apparent that the center (x_0, y_0) of the epicycle drifts at a constant speed $(\dot{x}_0, \dot{y}_0 - q\Omega_0 x_0) = [R_0(\Omega_0 - \Omega_p) \sin i, R_0(\Omega_0 - \Omega_p) - q\Omega_0 x_0]$ due to the background velocity \mathbf{v}_0 (Equation (1)) in the spiral-arm coordinates.

As an example, we take $\Omega_p = \Omega_0/2$, $\sin i = 0.2$, $q = 1$, and $L_x = \pi \sin i R_0$, and initially consider a star particle located at $(x, y)/L_x = (0, 3.80)$ with velocity $(\dot{x}, \dot{y})/(\Omega_0 L_x) = (2.96, 1.59)$ at $t = 0$, corresponding to $a\Omega_0/L_x = 1.4$, $b = x_0 = 0$, and $y_0/L_x = 1$. We integrate Equation (A9) with $\Phi_1 = 0$ using a kick-drift-kick scheme of the leap-frog integrator suggested by Quinn et al. (2010), with a time step of $\Delta t = 10^{-3}/\Omega_0$. Figure 26 plots the temporal changes of the orbit, the relative errors in the energy $\delta E/E$ and the position offset $\delta s/y$ between the numerical and analytic solutions (Equation (A11)), and the trajectory in the x - y plane. As expected, the stellar orbit consists of an epicycle motion in the clockwise direction and a constant drift of its guiding center indicated by the dotted lines. The energy is conserved within 0.1%, while the position offset is less than 0.6%.

REFERENCES

- Baba, J., Morokuma-Matsui, K., & Saitoh, T. R. 2017, MNRAS, 464, 246
- Balbus, S. A. 1988, ApJ, 324, 60
- Balbus, S. A., & Cowie, L. L. 1985, ApJ, 297, 61
- Beck, R. 2016, A&A Rev., 24, 4
- Bigiel, F., Leroy, A., Walter, F., et al. 2008, AJ, 136, 2846
- Bolatto, A. D., Wong, T., Utomo, D., et al. 2017, ApJ, 846, 159
- Boulares, A., & Cox, D. P. 1990, ApJ, 365, 544
- Bovy J., Rix H.-W., Liu C., et al. 2012, ApJ, 753, 148
- Buta, R., & Combes, F. 1996, FCPH, 17, 95
- Cepa, J., & Beckman, J. E. 1990, ApJ, 349, 497
- Chandar, R., Chien, L.-H., Meidt, S., et al. 2017, ApJ, 845, 78
- Daniel K. J., & Wyse R. F. G., 2015, MNRAS, 447, 3576
- Daniel K. J., & Wyse R. F. G., 2018, MNRAS, 476, 1561
- Dobbs, C. L., Adamo, A., Few, C. G., et al. 2017, MNRAS, 464, 3580
- Dobbs, C., & Baba, J. 2014, PASA, 31, 35
- Dobbs, C. L., & Bonnell, I. A. 2006, MNRAS, 367, 873
- Dobbs, C. L., & Pringle, J. E. 2010, MNRAS, 409, 396
- Draine, B. T. 1978, ApJS, 36, 595
- Eden, D. J., Moore, T. J. T., Morgan, L. K., Thompson, M. A., & Urquhart, J. S. 2013, MNRAS, 431, 1587
- Eldridge, J. J., Langer, N., & Tout, C. A. 2011, MNRAS, 414, 3501
- Elmegreen, B. G. 1994, ApJ, 433, 39
- Elmegreen, B. G. 2011, in Star Formation in the Local Universe, EAS Publication Series, 51, 19
- Elmegreen, B. G., & Elmegreen, D. M. 1983, MNRAS, 203, 31
- Elmegreen, B. G., & Elmegreen, D. M. 1986, ApJ, 311, 554
- Elmegreen, B. G., & Elmegreen, D. M. 2019, ApJS, 245, 14
- Elmegreen, B. G., Elmegreen, D. M., & Efremov, Y. N., 2018, ApJ, 863, 59
- Elmegreen, D. M. 1980, ApJ, 242, 528
- Fletcher, A., Beck, R., Shukurov, A., Berkhuysen, E. M., & Horellou, C. 2011, MNRAS, 412, 2396
- Foyle K., Rix H.-W., Walter, F., & Leroy, A. K. 2010, ApJ, 725, 534
- Frick, P., Stepanov, R., Beck, R., et al. 2016, A&A, 585, 21
- Gammie, C. F. 2001, ApJ, 553, 174
- Gong, H., & Ostriker, E. C. 2013, ApJS, 204, 8
- Hawley, J. F., Gammie, C. F., & Balbus, S. A. 1995, ApJ, 440, 742
- Huber, D., & Pfenniger, D. 2001, A&A, 374, 465
- Hunter, J. D. 2007, CSE, 9, 90
- Iffrig, O., & Hennebelle, P. 2015, A&A, 576, 95
- Kaleida, C., & Scowen, P. A. 2010, ApJ, 140, 379
- Kennicutt, R. C., Jr. 1989, ApJ, 344, 685
- Kennicutt, R. C., Jr. 1998, ApJ, 498, 541
- Kim, C.-G., Kim, W.-T., & Ostriker, E. C. 2008, ApJ, 681, 1148
- Kim, C.-G., Kim, W.-T., & Ostriker, E. C. 2011, ApJ, 743, 25
- Kim, C.-G., Ostriker, E. C., & Kim, W.-T. 2013, ApJ, 776, 1
- Kim, C.-G., & Ostriker, E. C. 2015a, ApJ, 802, 99
- Kim, C.-G., & Ostriker, E. C. 2015b, ApJ, 815, 67
- Kim, C.-G., & Ostriker, E. C. 2017, ApJ, 846, 133
- Kim, C.-G., & Ostriker, E. C. 2018, ApJ, 853, 173
- Kim, W.-T., Kim, Y., & Kim, J.-G. 2014, ApJ, 789, 68
- Kim, W.-T., & Ostriker, E. C. 2001, ApJ, 559, 70
- Kim, W.-T., & Ostriker, E. C. 2002, ApJ, 570, 132
- Kim, W.-T., & Ostriker, E. C. 2006, ApJ, 646, 213
- Kim, W.-T., & Ostriker, E. C. 2007, ApJ, 660, 1232

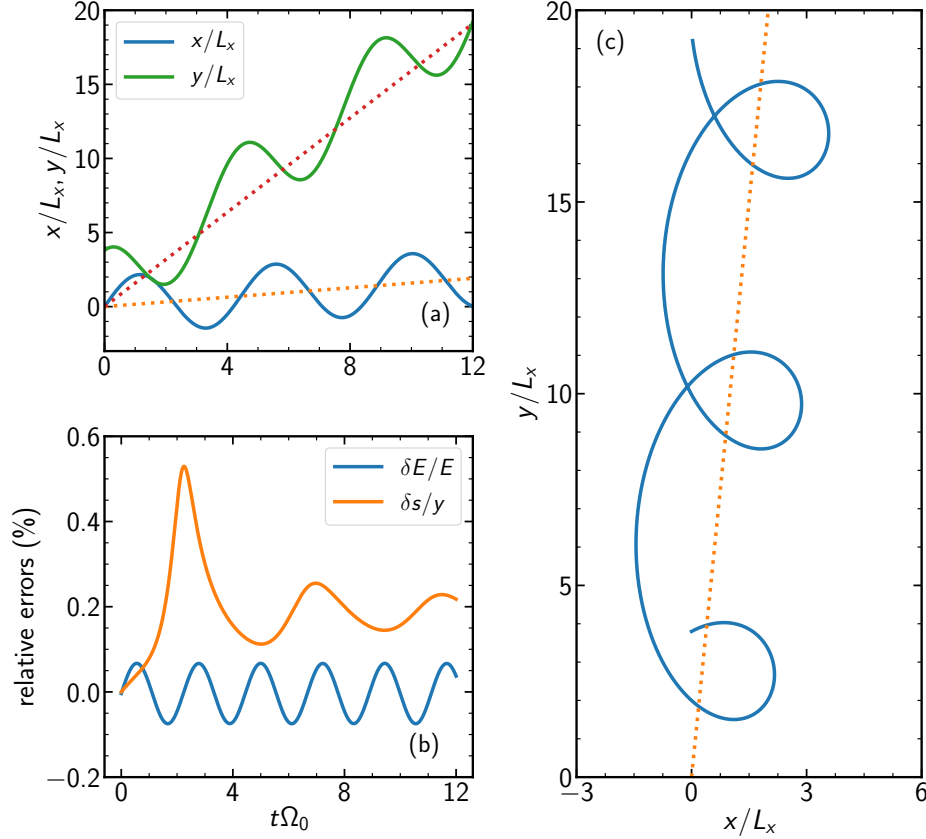


Figure 26. Illustration of a particle orbit with the initial conditions $(x, y)/L_x = (0, 3.80)$ and $(\dot{x}, \dot{y})/(\Omega_0 L_x) = (2.96, 1.59)$ at $t = 0$, calculated from integrating Equation (A9) with $\Phi_1 = 0$. Temporal changes of (a) the x - and y -coordinates of the particle and (b) the relative errors in the energy $\delta E/E$ and the position offset δs between the numerical and analytic results. (c) The trajectory of the particle orbit in the x - y plane. In (a) and (c), the dotted lines draw the movement of the guiding center of the epicycle.

- Kim, Y., Kim, W.-T., & Elmegreen, B. G. 2015, *ApJ*, 809
- Knapen, J. H., Beckman, J. E., Cepa, J., & Nakai, N. 1996, *A&A*, 308, 27
- Koo, B.-C., Park, G., Kim, W.-T., et al. 2017, *PASJ*, 129, 094102
- Kormendy, J., & Kennicutt, R. C. 2004, *ARA&A*, 42, 603
- Koyama, H., & Inutsuka, S.-i. 2002, *ApJ*, 564, L97
- Koyama, H., & Ostriker, E. C. 2009, *ApJ*, 693, 1316
- Kreckel, K., Faesi, C., Kruijssen, M. M. D., et al. 2018, *ApJ*, 863, L21
- Kroupa, P. 2001, *MNRAS*, 322, 231
- Krumholz, M. R., Bate, M. R., Arce, H. G., et al. 2014, in *Protostars and Planets VI*, ed. H. Beuther et al. (Tucson, AZ: Univ. Arizona Press), 243
- Kuijken, K., & Gilmore, G. 1989, *MNRAS*, 239, 571
- La Vigne, M. A., Vogel, S. N., & Ostriker, E. C. 2006, *ApJ*, 650, 818
- Lee, W.-K. 2014, *ApJ*, 792, 122
- Lee, W.-K., & Shu, F. H. 2012, *ApJ*, 756, 45
- Lehner, N., & Howk, J. C. 2011, *Science*, 334, 955
- Leitherer, C., Schaerer, D., Goldader, J. D., et al. 1999, *ApJS*, 123, 3
- Leroy, A. K., Schinnerer, E., Hughes, A., et al. 2017, *ApJ*, 846, 71
- Leroy, A. K., Walter, F., Brinks, E., et al. 2008, *AJ*, 136, 2782
- Leroy, A. K., Walter, F., Sandstrom, K., et al. 2013, *AJ*, 146, 19
- Lin, C. C., & Shu, F. H. 1964, *ApJ*, 140, 646
- Lin, C. C., & Shu, F. H. 1966, *PNAS*, 55, 229
- Lord, S. D., & Young, J. S. 1990, *ApJ*, 356, 135
- Lynds, B. T. 1970, in *IAU Symp. 38, The Spiral Structure of Our Galaxy*, ed. W. Becker & G. I. Contopoulos (Dordrecht: Reidel), 26
- Mac Low, M.-M., & Klessen, R. S. 2004, *RvMP*, 76, 125
- Martizzi, D., Faucher-Giguère, C.-A., & Quataert, E. 2015, *MNRAS*, 450, 504
- McCrack, R., & Snow, T. P. 1979, *ARA&A*, 17, 213
- McKee, C. F., & Ostriker, E. C. 2007, *ARA&A*, 45, 565
- McKinney, W. 2010, in *Proc. 9th Python in Science Conf., Data Structures for Statistical Computing in Python*, ed. S. van der Walt & J. Millman (Austin, TX: SciPy), 51
- Muraoka, K., Kohno, K., Tosaki, T., et al. 2009, *ApJ*, 706, 1213
- Ostriker, E. C., McKee, C. F., & Leroy, A. K. 2010, *ApJ*, 721, 975
- Ostriker, E. C., & Shetty, R. 2011, *ApJ*, 731, 41
- Pérez, F., & Granger, B. E. 2007, *CSE*, 9, 21
- Pettitt, A. R., Tasker, E. J., Wadsley, J. W., Keller, B. W., & Benincasa, S. M. 2017, *MNRAS*, 468, 4189
- Piontek, R. A., & Ostriker, E. C. 2007, *ApJ*, 663, 183
- Puerari, I., Elmegreen, B. G., & Block, D. L. 2014, *AJ*, 148, 133
- Putman, M. E., Peek, J. E. G., & Jounge, M. R. 2012, *ARA&A*, 50, 491
- Quinn, T., Perrine, R. P., Richardson, D. C., & Barnes, R. 2010, *AJ*, 139, 803
- Rand, R. J. 1993, *ApJ*, 410, 68
- Renaud, F., Bournaud, F., Emsellem, E., et al. 2013, *MNRAS*, 436, 1836
- Roberts, W. W. 1969, *ApJ*, 158, 123
- Roberts, W. W., Roberts, M. S., & Shu, F. M. 1975, *ApJ*, 196, 381
- Roškar, R., Debattista, V. P., Quinn, T. R., Stinson, G. S., & Wadsley, J. 2008, *ApJ*, 684, L79
- Sandage, A. 1961, *The Hubble Atlas of Galaxies* (Washington D.C.: Carnegie Institution)
- Schinnerer, E., Meidt, S. E., Pety, J., et al. 2017, *ApJ*, 836, 62
- Schinnerer, E., Meidt, S. E., Colombo, D., et al. 2017, *ApJ*, 836, 62
- Schmidt, M. 1959, *ApJ*, 129, 243
- Schruba, A., Leroy, A. K., Walter, F., et al. 2011, *AJ*, 142, 37
- Scoville, N. Z., Polletta, M., Ewald, S., et al. 2001, *AJ*, 122, 3017
- Seigar, M. S., & James, P. A. 2002, *MNRAS*, 337, 1113
- Sellwood, J. A. 2014, *RvMP*, 86, 1
- Shabani, F., Grebel, E. K., Pasquali, A., et al. 2018, *MNRAS*, 478, 3590

- Shetty, R., & Ostriker, E. C. 2006, *ApJ*, 647, 997
- Shetty, R., & Ostriker, E. C. 2008, *ApJ*, 684, 978
- Shetty, R., & Ostriker, E. C. 2012, *ApJ*, 754, 2
- Shu, F. H. 2016, *ARA&A*, 54, 667
- Shu, F. H., Milione, V., & Roberts, W. W. 1973, *ApJ*, 183, 819
- Sormani, M. C., Sobacchi, E., Shore, S. N., Treß, R. G., & Klessen, R. S. 2017, *MNRAS*, 471, 2932
- Stepanov, R., Shukurov, A., & Fletcher, A., et al. 2014, *MNRAS*, 437, 2201
- Sternberg, A., McKee, C. F., & Wolfire, M. G. 2002, *ApJS*, 143, 419
- Stone, J. M., Gardiner, T. A., Teuben, P., Hawley, J. F., & Simon, J. B. 2008, *ApJS*, 178, 137
- Sutherland, R. S., & Dopita, M. A. 1993, *ApJS*, 88, 253
- Tabatabaei, F.S., Schinnerer, E., Murphy, E. J., et al. 2013, *A&A*, 552, 19
- Tomisaka, K., Habe, A., & Ikeuchi, S. 1981, *Ap&SS*, 78, 273
- Tress, R. G., Smith, R. J., Sormani, M. C. et al. 2020, *MNRAS*, 492, 2973
- van der Walt, S., Colbert, S. C., & Varoquaux, G. 2011, *CSE*, 13, 22
- Van Eck, C. L., Brown, J. C., Shukurov, A., & Fletcher, A. 2015, *ApJ*, 799, 35
- Wada, K., & Koda, J. 2004, *MNRAS*, 349, 270
- Walch, S., & Naab, T. 2015, *MNRAS*, 451, 2757
- Webb, G. M., & Mace, R. L. 2015, *JPIPh*, 81, 905810115
- Wong, T. & Blitz, L. 2002, *ApJ*, 569, 157